

# JGR Oceans

## RESEARCH ARTICLE

10.1029/2024JC022100

### Special Collection:

Regional Sea Level Change and Society

### Key Points:

- Regional patterns of sea level change are investigated using satellite observations and large ensembles of global coupled climate models
- Wind forcing—Ekman and Sverdrup dynamics in particular—played a key role in shaping sea level changes in different regions since 1993
- Much of the observed pattern is captured by climate models driven by anthropogenic forcings; single-forcing runs enable further attribution

### Supporting Information:

Supporting Information may be found in the online version of this article.

### Correspondence to:

K. B. Karnauskas,  
[kristopher.karnauskas@colorado.edu](mailto:kristopher.karnauskas@colorado.edu)

### Citation:

Karnauskas, K. B., Nerem, R. S., Fasullo, J. T., Bellas-Manley, A., Thompson, P. R., Coats, S., et al. (2025). Diagnosing regional sea level change over the altimeter era. *Journal of Geophysical Research: Oceans*, 130, e2024JC022100. <https://doi.org/10.1029/2024JC022100>

Received 8 NOV 2024

Accepted 2 JUN 2025

### Author Contributions:

**Conceptualization:** Kristopher B. Karnauskas, R. Steven Nerem, John T. Fasullo, Philip R. Thompson, Sloan Coats, Don P. Chambers, Benjamin D. Hamlington  
**Formal analysis:** Kristopher B. Karnauskas, Ashley Bellas-Manley  
**Funding acquisition:** R. Steven Nerem, John T. Fasullo  
**Investigation:** Kristopher B. Karnauskas  
**Methodology:** Kristopher B. Karnauskas  
**Visualization:** Kristopher B. Karnauskas  
**Writing – original draft:** Kristopher B. Karnauskas

© 2025. American Geophysical Union. All Rights Reserved.

## Diagnosing Regional Sea Level Change Over the Altimeter Era

Kristopher B. Karnauskas<sup>1,2</sup> , R. Steven Nerem<sup>2,3</sup> , John T. Fasullo<sup>1,4</sup> , Ashley Bellas-Manley<sup>3</sup> , Philip R. Thompson<sup>5</sup> , Sloan Coats<sup>6</sup>, Don P. Chambers<sup>7</sup> , and Benjamin D. Hamlington<sup>8</sup> 

<sup>1</sup>Department of Atmospheric and Oceanic Sciences, University of Colorado Boulder, Boulder, CO, USA, <sup>2</sup>Cooperative Institute for Research in Environmental Sciences, University of Colorado Boulder, Boulder, CO, USA, <sup>3</sup>Smead Aerospace Engineering Sciences, Colorado Center for Astrodynamics Research, University of Colorado Boulder, Boulder, CO, USA, <sup>4</sup>Climate and Global Dynamics Laboratory, National Center for Atmospheric Research, Boulder, CO, USA, <sup>5</sup>Department of Oceanography, University of Hawai'i at Mānoa, Honolulu, HI, USA, <sup>6</sup>Department of Earth Sciences, University of Hawai'i at Mānoa, Honolulu, HI, USA, <sup>7</sup>College of Marine Science, University of South Florida, St. Petersburg, FL, USA, <sup>8</sup>Jet Propulsion Laboratory, California Institute of Technology, Pasadena, CA, USA

**Abstract** Since 1993, satellite altimeters have been mapping sea level changes globally, revealing both the global mean rate and detailed patterns of regional variations. The global mean rate is well studied, closely linked to global energy and water cycles, while regional patterns are influenced by a complex mix of internal climate dynamics and external factors like greenhouse gases and aerosols. Yet, a synthesis of these regional patterns using a comprehensive diagnostic approach has been lacking. Our research addresses this gap by integrating oceanic and atmospheric observations with large ensembles of state-of-the-art global climate models. This approach sheds new light upon the mechanisms behind basin-scale sea level patterns worldwide. A key finding is the dominant influence of wind forcing, particularly Ekman and Sverdrup dynamics, in shaping sea level changes from the tropics to higher latitudes. We find that the pattern of sea level rise since 1993 is primarily driven by wind-induced changes in ocean circulation, which can affect sea surface height through ocean mass and heat distribution. Interestingly, these wind-driven changes are not just products of internal climate variability; most of the observed patterns are recovered by global climate model projections driven by historical anthropogenic forcings, and single-forcing experiments provide further insight into which forcings are responsible for various features in the satellite altimetry record. Understanding the drivers of regional sea level rise, including differentiating anthropogenic signals from natural variability, is essential for effectively adapting to climate change impacts on global infrastructure and society.

**Plain Language Summary** Since 1993, satellites have been tracking changes in global sea levels, revealing both overall trends and regional variations. The overall rate of global sea level rise is closely tied to the Earth's energy and water systems. However, we have lacked a comprehensive understanding of the regional variations and the factors influencing them. Our study aimed to fill this gap by combining oceanic and atmospheric observations with advanced climate models. Through this approach, we have shed new light upon the main drivers of sea level patterns in different regions worldwide. One significant finding is that wind patterns play a dominant role in shaping sea level changes from the tropics to higher latitudes through their impact on the ocean circulation, which in turn redistributes ocean mass and heat. Interestingly, a substantial portion of these wind-driven changes can be attributed to human influences, as demonstrated by our climate model simulations. Understanding the reasons behind regional sea level rise, including distinguishing between natural variability and human-induced changes, is crucial for adapting to the impacts of climate change on global infrastructure and society.

## 1. Introduction

Sea level is both an indicator of climate change, and a diagnostic of the ocean circulation. It reflects the volume and heat content of the ocean (including variations in thermocline depth, particularly in the tropics and subtropics), and its horizontal gradients are associated with surface currents through geostrophic balance. Since 1993, the global average sea level has risen by about 0.1 m (~3.4 mm per year). Locally, however, relative sea level rise totals in the altimeter record are as high as 0.9 m and as low as -0.4 m (Figure 1a), with a global standard deviation of 0.4 m (at 0.25° horizontal resolution). The time-mean height of the sea surface relative to the geoid (or

Writing – review & editing: Kristopher B. Karnauskas, R. Steven Nerem, John T. Fasullo, Ashley Bellas-Manley, Philip R. Thompson, Sloan Coats, Don P. Chambers, Benjamin D. Hamlington

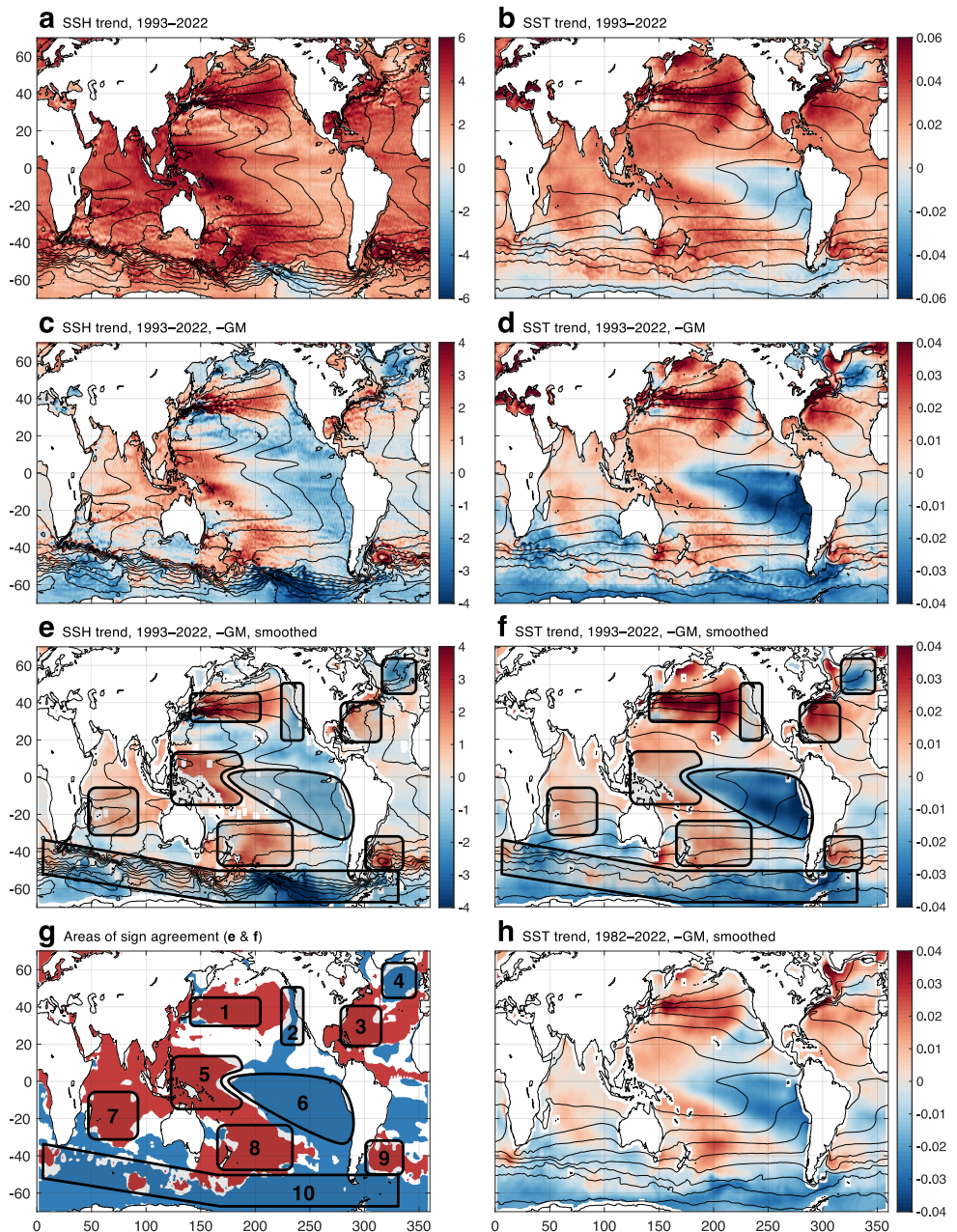


**Figure 1.** Global SSH and sea surface temperature (SST) trends. (a) Observed linear trend in SSH from 1993 to 2022 (mm/yr) along with the MDT field (contoured every 0.2 m). (b) As in a but for SST ( $^{\circ}\text{C}/\text{yr}$ ) with the annual mean SST (contoured every  $4^{\circ}\text{C}$ ). (c and d) As in panels (a and b) but with the global mean trends removed ( $70^{\circ}\text{S}$ – $70^{\circ}\text{N}$ , area-weighted). (e and f) As in panels (c and d) but smoothed with a  $4^{\circ}$  latitude by longitude spatial filter and several regions identified as discussed in the main text. (g) Areas in which the signs of SSH and SST trends (relative to global mean, smoothed) are in agreement. (h) As in f but for the period 1982–2022. Nearly the entirety of the SSH and SST trend maps ((a) and (b) as well as b but for the period 1982–2022) are significant at the 95% confidence level (Figure S2 in Supporting Information S1).

mean dynamic topography, MDT) varies by about 3 m from the top of the westward-intensified North Pacific gyre near the Kuroshio Current to its lowest point in the Southern Ocean near the Antarctic Circumpolar Current. Therefore, the observed regional variations in sea level rise are significant in terms of the dynamics of the global ocean circulation.

Sea level rise also poses substantial risks to coastal communities, where the impacts are intensified by regional patterns influenced by ocean circulation dynamics. These patterns, which maybe driven by wind-induced changes

and oceanic responses such as those set by Ekman and Sverdrup dynamics, create spatially varied sea level trends that can result in “hotspots” of accelerated rise or even localized decreases. The societal implications of these variations are significant, especially for coastal infrastructure, freshwater resources, and ecosystems, which are sensitive to even modest changes in relative sea level (Nicholls & Cazenave, 2010; Sweet et al., 2017). By deepening our understanding of the interplay between ocean circulation and regional sea level patterns, this research aims to inform targeted adaptation strategies that address the unique vulnerabilities of different regions. In particular, understanding the mechanisms driving regional differences, such as western boundary currents and tropical Pacific dynamics, can lend overall confidence to adaptation planning for the most impacted communities.

The challenge of understanding the regional patterns of sea level rise is not distinct from that of the spatial heterogeneity of climate change more broadly, including both surface and subsurface warming (Fasullo & Gent, 2017). For example, over the altimeter-era (since 1993), there is a high degree of alignment between sea surface height (SSH) and sea surface temperature (SST) trends at regional scales (Figures 1a–1g). The pattern correlation between the spatially smoothed SSH and SST trends (Figures 1e and 1f) is 0.68%, and 76% of the global ocean surface area (between 70°S and 70°N) agrees on the sign of SSH and SST trends (Figure 1g). Some of the area of disagreement is where trend values are smaller; when excluding trend values less than 10% of the mean absolute value of each trend field, 80% of the ocean surface agrees on the sign. However, cause and effect cannot be inferred from such statistics alone. For example, it maybe reasonable to assume that SST warming reflects an accumulation of heat, which leads to rising SSH. On the other hand, a local rise in SSH may reflect an accumulation of mass driven by changes in surface wind stress (via Ekman or Sverdrup dynamics), and changes in SSH can alter the surface ocean circulation through geostrophic balance, which can subsequently advect temperature or mixed layer depth anomalies. The mechanisms for SSH trends (relative to the global mean) likely vary by region, and a closer investigation of their relationship with other climate variables such as wind and SST is necessary to understand them. Indeed, some of the most striking patterns of SSH (and SST) change since 1993 are in tightly coupled regions—the tropical Pacific, for example—rendering this challenge a general climate dynamics problem not unique to the science of sea level rise.

Several studies highlight the emergence of regional patterns of sea level rise during the altimeter-era, and conclude that they are driven significantly by anthropogenic forcing (Camargo et al., 2022; Fasullo & Nerem, 2018; Hamlington et al., 2019; Samanta et al., 2024; Stammer et al., 2013; Walker et al., 2021). Timmermann et al. (2010), Thompson et al. (2016), and Han et al. (2018) discuss the role of wind regimes and ocean dynamics, particularly in the southern Indo-Pacific Ocean and equatorial ocean/North Indian Ocean, in shaping regional sea level trends. In the tropical Pacific, the impact of regional modes of climate variability such as the Pacific decadal oscillation and El Niño-Southern Oscillation is noted by Sérazin et al. (2016), Peyser et al. (2016), and Royston et al. (2018), suggesting a strong interplay between ocean-atmosphere dynamics and sea level changes. A major theme across these papers is the effort to distinguish between natural variability and anthropogenic influences on sea level trends. Studies by Fasullo et al. (2020a, 2020b) and Richter et al. (2020) employ climate models to detect the anthropogenic signal amid the natural variability. They find that recent sea level trends cannot be fully explained by natural factors alone, indicating a significant human-induced component. This conclusion is reinforced by Dangendorf et al. (2023) and Domingues et al. (2018), who attribute recent accelerations in sea level rise along the U.S. coasts to a combination of natural variability and human influence.

The future trajectory of sea level rise and its regional disparities is a common concern. Studies by Hamlington et al. (2021) and Ezer (2019) discuss the ongoing challenges in predicting future sea level changes, especially given the current limitations in separating natural variability from anthropogenic influences. Sallenger et al. (2012) and Schloesser et al. (2021) highlight the “hotspots” of accelerated sea level rise, stressing the need for region-specific studies to better understand and prepare for future sea level scenarios. These studies underscore the complexity of regional sea level rise, driven by a combination of natural and anthropogenic factors, and highlight the importance of improving our understanding of these dynamics to better predict and adapt to future changes.

Furthermore, Todd et al. (2020) underscore the role of ocean circulation and mixing changes in shaping regional sea level and heat content patterns with significant implications for understanding future sea level rise and its regional variations. By investigating the ocean response to surface flux perturbations, they highlight substantial model disagreement in regional sea level and ocean heat content changes. Bronselaer and Zanna (2020) suggest that future ocean warming patterns might become more predictable as the climate warms because of the stability

of preindustrial circulation patterns by establishing a linear relationship between heat and carbon uptake in response to anthropogenic emissions, primarily determined by intrinsic parameters of the Earth system. Overall, these studies reveal the impact of changes in ocean circulation on ocean warming patterns in observations and global models, which can likewise influence patterns of sea level rise.

The aim of this paper is to shed light onto the physical mechanisms for the key features of the global patterns of relative sea level rise, and through consideration of those mechanisms as well as comparison with global climate model experiments, consider the problem of attribution. Although this study focuses primarily on the satellite altimeter-era, which began in 1993, the results maybe applicable further back in time than 1993. For example, it is worth noting that the spatial pattern of SST trends since 1993 is very similar to that since 1982, with a spatial correlation of 0.92 (Figures 1f and 1h). Therefore, it would be unlikely that the SSH trends would look entirely different if the altimeter record began in 1982.

## 2. Data and Methods

### 2.1. Observations

To characterize the spatial patterns of altimeter-era sea level rise, we use the NASA Jet Propulsion Laboratory (JPL) Making Earth System Data Records for Use in Research Environments (MEASUREs) Gridded Sea Surface Height Anomalies Version 2205 (Fournier et al., 2022), covering the complete 30-year period 1993–2022 with a spatial resolution of 1/6° every five days. The JPL data set integrates measurements from many satellite missions including TOPEX/Poseidon, Jason-1, Jason-2, Jason-3, Jason-CS (Sentinel-6), ERS-1, ERS-2, Envisat, SARAL-AltiKa, CryoSat-2, Sentinel-3A, and Sentinel-3B using Kriging interpolation. All linear trends are calculated by ordinary least squares regression; this applies to sea level, SST, and winds.

Although not shown, to ensure robustness of our results, we repeat all sea level analyses using the monthly, 0.25°-resolution “Global Ocean Gridded Level 4 (L4) Sea Surface Heights (SSH) And Derived Variables Reprocessed 1993 Ongoing” data set spanning 1993–2022 (CMEMS, 2023). The CMEMS data set uses an optimal interpolation (OI) technique to merge the Level 3 (L3) along-track measurements from all available satellite altimeter missions including most of those mentioned above for the JPL data set, plus GeoSat Follow-On and HaiYang-2A, and is processed by the Data Unification and Altimeter Combination System (DUACS) multimission altimeter data processing system. CMEMS sea level anomalies are computed relative to a 20-year mean (1993–2012).

To provide relevant spatial context to regional trends in sea level, the time-mean SSH relative to the geoid (MDT) is plotted on several figures. We use the Archiving, Validation and Interpretation of Satellite Oceanographic data (AVISO) combined mean dynamic topography (MDT CNES-CLS22) product (Joussot et al., 2022), which is an estimate of MDT over 1993–2012 at 1/8° resolution (consistent with the base period of DUACS products such as the CMEMS data set).

For comparisons with SST, the monthly, high-resolution (0.25°) version of the NOAA Optimal Interpolation version 2 (OIV2) is used (Huang et al., 2021). The OIV2 data set blends infrared satellite retrievals from the Advanced Very High Resolution Radiometer and in situ measurements from the International Comprehensive Ocean Atmosphere Data Set. While the OIV2 data set begins in 1982, trends are also computed over 1993–2022 to match the altimeter record.

To investigate the role of wind forcing in shaping the altimeter-era patterns of sea level rise, we use ERA5, the fifth generation atmospheric reanalysis from the European Centre for Medium-Range Weather Forecasts (ECMWF) (Hersbach et al., 2020). We use monthly, 0.25°-resolution surface wind stress fields from ERA5 spanning 1993–2022. To ensure consistency, we repeat calculations using monthly wind stress from the 0.5°-resolution NASA Modern-Era Retrospective analysis for Research and Applications version 2 (MERRA-2) (Gelaro et al., 2017) over the same time period (not shown).

Several calculations are made using the aforementioned wind stress data sets, which enable diagnosis of changes in the wind-driven ocean circulation and their potential impact on spatial patterns of sea level rise. Standard diagnostics include Ekman pumping velocity ( $w_{Ek} = \frac{1}{\rho} \nabla \times \vec{\tau}$ ), Sverdrup stream function ( $\psi_{Sv} = \frac{1}{\rho \beta} \int_{x_e}^x \nabla \times \vec{\tau} dx$ ), Sverdrup transport ( $M_{Sv}^y = \frac{1}{\rho \beta} \nabla \times \vec{\tau} \approx -\frac{1}{\rho \beta} \frac{\partial \tau_x}{\partial y}$ ), and the meridional convergence of Sverdrup transport ( $-\frac{\partial M_{Sv}^y}{\partial y} = \frac{\partial}{\partial y} \left( \frac{1}{\rho \beta} \frac{\partial \tau_x}{\partial y} \right)$ ), where  $\rho$  is a reference seawater density ( $1,025 \text{ kg m}^{-3}$ ),  $\vec{\tau}$  is the surface

wind stress vector,  $f$  is the Coriolis parameter ( $7.3 \cdot 10^{-5} \text{ s}^{-1}$ ), and  $\beta$  is the beta parameter ( $\frac{\partial f}{\partial y}$ ). Ekman pumping velocity illuminates the role of steady, wind-driven vertical motions and their effect on the thermocline, while the Sverdrup relation (in its various expressions above) embodies the forced, steady, barotropic, and linear potential vorticity balance. As such, the meridional *convergence* of Sverdrup transport sheds light onto the accumulation of mass—particularly as a function of latitude.

## 2.2. Numerical Models

This study makes use of several models—two generations of the National Center for Atmospheric Research (NCAR) Community Earth System Model (CESM)—a fully coupled climate model with interactive ocean and atmosphere, an atmosphere-only version of the CESM that is forced by prescribed SST fields (also known as an atmospheric general circulation model), and a simple barotropic ocean model.

For an additional layer of dynamical insight into the role of wind forcing in shaping the patterns of sea level rise, observed (or simulated by a different model) trends in wind stress  $\vec{\tau}$  maybe used as forcing to a simple ocean model that numerically solves the barotropic vorticity equation,  $\frac{\partial \zeta}{\partial t} + \frac{\partial u}{\partial x} \frac{\partial \zeta}{\partial y} - \frac{\partial u}{\partial y} \frac{\partial \zeta}{\partial x} + \beta \frac{\partial u}{\partial x} = \nabla \times \vec{\tau} - \epsilon \zeta + \nu \nabla^2 \zeta$ . The vorticity equation is essentially Sverdrup balance ( $\beta \frac{\partial u}{\partial x} = \nabla \times \vec{\tau}$ ) plus advection (of relative vorticity). The second and third terms on the left-hand side of the barotropic vorticity equation represent advection, since  $u = -\frac{\partial \psi}{\partial y}$  and  $v = \frac{\partial \psi}{\partial x}$ . Such a model may also include simple parameterizations of dissipation in the form of bottom drag  $\epsilon$  and lateral viscosity  $\nu$ . In this model, the lateral viscosity coefficient is set to  $3 \times 10^8 \text{ m}^2/\text{s}$  and bottom drag is neglected (a constant depth of 4 km is used). The model is integrated with a time step of 1 minute via centered difference with leapfrog. Being a simple barotropic model subject only to constant wind forcing, a steady solution is reached quite rapidly; the results presented are taken as averages of time steps 800–1,000. The model domain crudely approximates the tropical and extratropical Pacific Ocean (60°S–60°N and 115° longitude wide) with a horizontal resolution of 0.25°. The vorticity field  $\zeta(x, y)$  is inverted to yield the barotropic stream function  $\psi(x, y)$  by the method of successive over-relaxation, which is analyzed in several figures in this paper.

The observed regional patterns of sea level rise, and those predicted by simple models such as the one described above, maybe compared with fully coupled global climate model simulations, and attributed to particular forcings using the “all forcing” (LE) and “single forcing” (SF) experiments from large ensembles of the NCAR CESM1 (Hurrell et al., 2013) and CESM2 (Danabasoglu et al., 2020). For reference, NCAR’s CESM1 and CESM2 were contributors to the Coupled Model Intercomparison Project phases 5 and 6 (CMIP5 and CMIP6), respectively. In this study, we analyze SSH and wind stress (TAUX and TAUY) outputs from these two models. For CESM1, we use 32 members (2–33) of the LE/all forcing ensemble and 20 members (1–20) of the SF experiment—focusing on the SF experiment isolating the impact of greenhouse gases (XGHG). These simulations span 1920–2080 (with historical forcing through 2005 and RCP8.5 forcing from 2006 onward) with resolution approximately 1° (Deser et al., 2020; Kay et al., 2015). The CESM2 experiments analyzed have similar specifications, but with some important differences in terms of parameterizations and process representation, ensemble size and initialization procedure, and forcing protocols as described by Rodgers et al. (2021). For the “all forcing” (LE) experiment of CESM2, we use the smoothed biomass burning (SMBB; Fasullo et al., 2022) ensemble with 50 members, which uses SSP370 forcing from 2015 onward. For the SF experiment, there are 15 ensemble members, and again, we focus on the one that isolates the role of greenhouse gases (GHG). It is important to note that the CESM1 SF experiment used an “all-but-one” method (i.e., the XGHG experiment was forced by all forcings *except* greenhouse gases), whereas the CESM2 SF experiment used the “only” method (i.e., the GHG experiment held all forcings constant at 1,850 levels *except* for greenhouse gases). Therefore, while the algebra necessary to isolate the response attributable to greenhouse gases is different between CESM1 and CESM2, the end results are directly comparable so long as aerosols are not the primary focus (Simpson et al., 2023).

Finally, experiments with an atmosphere-only version of CESM2—the CESM2-CAM6 global atmospheric model—are used to isolate the impact of enhanced SST warming in the eastern tropical Pacific. These experiments, the full methodology of which is described in Karnauskas et al. (2023), involve two sets of simulations: one in which the full SST trend simulated by the coupled version of CESM2 is imposed to the atmospheric as boundary forcing (“EP”) and one that is the same but with the enhanced SST warming in the eastern tropical Pacific suppressed (“noEP”). Each experiment includes five ensemble members of the atmospheric model driven

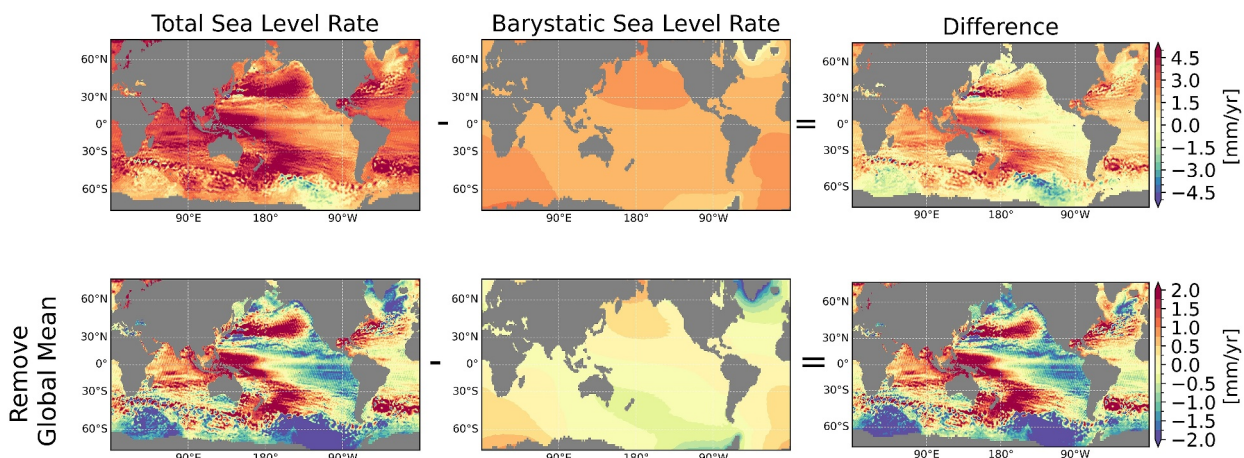


**Figure 2.** Effect of geodesy on regional patterns of sea level rise. The total sea level rate based on satellite altimeter data spanning 1993–2022 (left), the barystatic sea level rate based on mass loss from ice sheets and glaciers over the altimeter-era (center), and the difference between them (i.e., the sterodynamic sea level rate) (right). In the bottom row, the global mean value has been removed from each panel to highlight the regional pattern. All results are expressed in terms of geocentric sea level rate in 2008.0 (the midpoint of the altimeter data record).

by prescribed SST forcing from 2015 through 2100. An ensemble mean is formed from each experiment to average out internal atmospheric variability and reveal the forced response.

We note that coupled global climate models such as those used here do not incorporate effects related to the gravitational, deformational and rotational (GRD) response of the Earth to present-day ice mass loss (i.e., present-day GRD; Gregory et al., 2019)—nor do they calculate global mean sea level. These effects influence regional sea level by altering the shape of the geoid and hence the distribution of ocean mass, formally known as the barystatic component of sea level (Coulson et al., 2022; Mitrovica et al., 2001, 2009; Tamisiea, 2011). However, the impact of present-day GRD from ice mass loss on the spatial pattern of sea level change is smaller than sterodynamic effects over the last 30 years (Figure 2). This is demonstrated by comparing the spatial patterns of total sea level change and barystatic sea level change over the altimeter-era.

We compute the rate of total sea level change from the combined multimission satellite altimeter record spanning 1993 through 2022 based on the *Jet Propulsion Lab MEaSUREs Gridded Sea Surface Height Anomalies Version 2205* (TOPEX/Poseidon, Jason-1, Jason-2, Jason-3, and Sentinel 6) (Fournier et al., 2022). We compute the rate at the midpoint of the record (2008.0) by applying a linear least squares fit of the function  $f(t) = b + rt + \frac{1}{2}at^2$  at each coordinate, where  $r$  is the rate. Then, we compute the rate of barystatic sea level change based on the GRD response of the Earth to surface loading from present-day ice mass loss. We construct a surface loading history that incorporates ice sheet mass loss from IMBIE data (Otosaka et al., 2023 and references therein), and glacier mass loss based on dynamic glacier evolution model PyGEM (Rounce et al., 2023) (Figure S1 in Supporting Information S1). Details of the model used to compute the present-day GRD effects are described by Paulson et al. (2005) and A et al. (2013), and details on the surface loading history can be found in Supporting Information S1 associated with this paper.

Results are expressed in terms of geocentric sea level, which is the shape of the sea surface relative to a fixed reference frame, consistent with satellite altimetry (Figure 2). While the barystatic component of sea level change is significant in terms of global mean, the pattern is long-wavelength and smoothly varying. We show that the pattern of sterodynamic sea level change (i.e., total sea level change minus barystatic sea level change, shown in the rightmost column of Figure 2) preserves the salient features of the regional total sea level pattern.

### 3. Results and Discussion

As mentioned in Section 1, the global distribution of relative sea level rise exhibits several coherent regional signals (Figure 1e), most of which (including ~80% of the global ocean surface) are coincident with same-signed regional trends in SST relative to its global mean (Figure 1f), where global mean throughout this paper is taken as the area-weighted mean over 70°S–70°N. Moreover, given the high degree of both hemispheric symmetry and

zonal asymmetry, many of these signals are hypothesized to be expressions of changes in key, regional components of the ocean circulation, the coupled ocean-atmosphere system, and other broadly studied climate phenomena. For example, the four major western boundary current systems exhibit markedly similar signs, magnitudes, and general patterns of change (labeled 1, 3, 8, and 9 on Figure 1g). Within the tropical Pacific, a clear zonal gradient of SSH (and SST) change emerges (labeled 5 and 6 on Figure 1g). This section pays visit to the salient features identified in Figure 1, and offers both diagnostic and attribution insights into their origins—What are their physical mechanisms including the role of atmospheric forcing, and are they part of the ocean's response to external radiative forcing?

### 3.1. Sharp Gradients Beget Large Trends When Displaced

Understandably, the most pronounced localized “hotspots” of sea level rise garner both scientific and societal attention (for example, <https://www.washingtonpost.com/climate-environment/interactive/2022/east-coast-sea-level-rise/>). Such hotspots with O (100-km) horizontal scale are found in several regions including near the major western boundary currents (Kuroshio and Gulf Stream) and in the Southern Ocean within the eddy-rich Agulhas Current System and elsewhere along the Antarctic Polar Front (APF) (Figure 1c). In the Kuroshio Extension region ~400 km off the coast of Japan, for example, sea level is rising by as much as 30 mm/yr—or about 10 times the global mean rate of sea level rise (Figure 3a). While these relatively small-scale features are undoubtedly important and potentially related to broader oceanographic changes and climatic forcings, we argue that their extreme amplitudes should not be surprising.

As demonstrated in Figure 3, such extreme rates of local sea level rise (positive or negative) are exclusively found along very sharp gradients in MDT. In such a setting, and by mathematical construction, even a subtle horizontal shift of the mean field will yield a very large local change. In the case of the Northern Hemisphere western boundary current extension regions, such horizontal shifts are phenomenologically equivalent to poleward shifts of the northern edges of the subtropical gyres, along with the western boundary currents that are dynamically constrained (by geostrophy) to those edges characterized by sharp MDT slopes. At the Kuroshio Extension along the northern edge of the Pacific subtropical gyre, for example, the MDT slope is approximately  $-0.3$  m per degree latitude (Figure 3b). This implies that the northern edge of the gyre need only migrate poleward by  $\sim 10$  km per year to account for a 30 mm/yr rate of local sea level rise there. Such migrations are reasonable when considering recent observed trends in the gyres (Yang et al., 2020). Indeed, poleward-shifting subtropical ocean gyres and concomitant changes in western boundary currents are an expected response to greenhouse gas forcing (Saenko et al., 2005; Seager & Simpson, 2016; Yang et al., 2016, 2020). Such shifts are directly attributable to changes in the extratropical atmospheric circulation—specifically the latitudinal distribution of zonal wind stress (*i.e.*, the wind stress curl) in the midlatitudes (Simpson et al., 2014), which is set by the width of the tropical belt and the Hadley circulation (Lu et al., 2007; Seidel et al., 2008), and systematically tied to the position of the jet stream and storm tracks (Yin, 2005). As the ocean gyres are trending poleward overall, there is inevitable small-scale variation or noise in that trend; exactly where along the gyre edges such movement occurs more or less within a 30-year period (yielding SSH trends like 30 mm/yr) is probably quite random and transient.

Finally, the negative SSH trend in the Pacific sector of the Southern Ocean is also found along a sharp latitudinal gradient in MDT (Figures 3e and 3f), which is referred to as the APF and is dynamically associated with the Antarctic Circumpolar Current. In this case, the local relation between the SSH trend and latitudinal MDT gradient implies a northward (or equatorward) shift of the APF in that region. Temporal variations in this crucial feature of the Southern Ocean circulation have been studied extensively (Dong et al., 2006; Freeman et al., 2016; Gille, 2014; Sokolov & Rintoul, 2009), and despite the heterogeneity in the SSH trends elsewhere along the APF, the observed changes are likely associated with wind-driven responses to the combined effects of increasing greenhouse gas and decreasing ozone concentrations (Fasullo et al., 2020; Lee & Feldstein, 2013). In all cases, whether positive or negative, the most pronounced local SSH trends in the world ocean are found in regions where such large local changes are possible with relatively modest shifts in the position of fundamental features of the basin-scale ocean circulation that happen to be characterized by sharp gradients in MDT.

### 3.2. Latitudinal Structure: The Sverdrup Perspective

As discussed in the previous section, changes in the global atmospheric circulation including the Hadley cells and jet stream are an expected response to anthropogenic radiative forcing, which impart changes in wind stress over

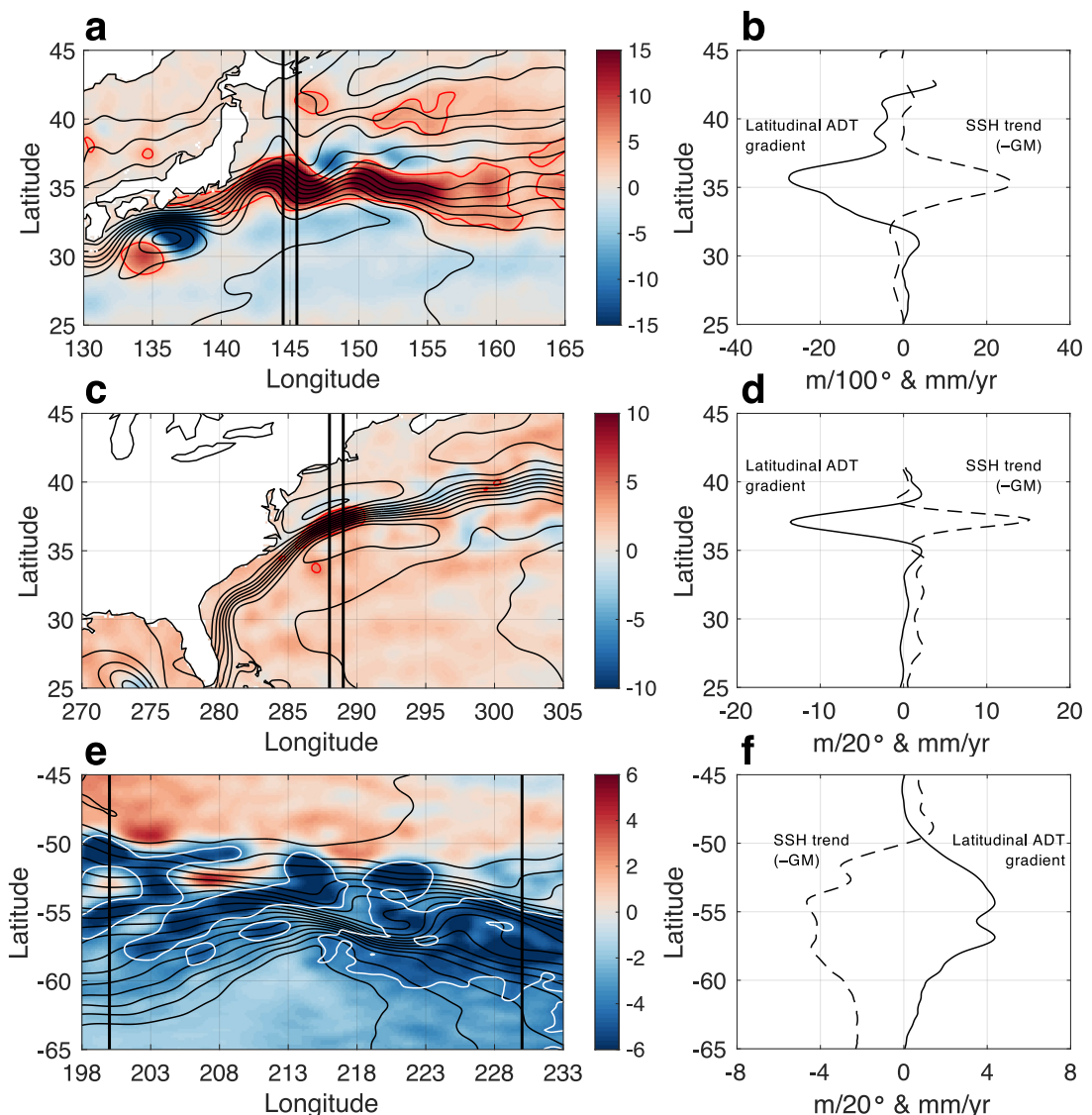


**Figure 3.** Largest SSH trends occur along sharp mean SSH gradients. (a) Observed linear trend in SSH from 1993 to 2022 relative to the global mean (taken throughout this paper as the area-weighted mean over 70°S–70°N) in the Kuroshio region (mm/yr) along with the MDT field (contoured every 0.1 m). The red contour outlines SSH trends exceeding 4 mm/yr. (b) Latitudinal profiles of the meridional gradient in MDT and the SSH trend along 145°E (a 1°-wide zonal mean as indicated in panel (a)). (c and d) As in panels (a and b) but for the Gulf Stream region. (e and f) As in panels (a and b) but for the Pacific sector of the Southern Ocean. In panel (e), the white contour outlines SSH trends less than -4 mm/yr; in panel (f), the profiles are calculated across a wider (30°) zonal distance. For clarity, the meridional MDT gradients in panels (b, c, and f) are scaled as noted in the x-axis label.

the ocean and therefore drive changes in the basin-scale ocean circulation (Seager & Simpson, 2016). The Sverdrup balance is a bedrock theory of wind-driven ocean circulation, particularly useful for interpreting midlatitude barotropic circulation; its associated diagnostics may thus lend insight into the observed patterns of sea level rise. Derived from the steady-state equations of motion in which only the wind stress, pressure gradient, and Coriolis forces are retained, the simplest form of the Sverdrup balance gives that the northward mass transport in the interior of the ocean will be proportional to the meridional gradient of zonal wind stress, with a negative sign  $\left(-\frac{\partial \tau_x}{\partial y}\right)$ . The *convergence* of meridional mass transport, then, is simply proportional to  $\frac{\partial}{\partial y} \left(\frac{\partial \tau_x}{\partial y}\right)$ .

The trend in Sverdrup transport convergence as computed from observed wind stress over 1993–2022 turns out to be a good predictor of the latitudinal structure of SSH trends over the same period (Figure 4). When the trend in Sverdrup transport convergence is computed from a profile of the trend in zonal wind stress averaged across the Pacific and compared to the SSH trend averaged across the Pacific (Figure 4b), the resulting correlation is 0.76

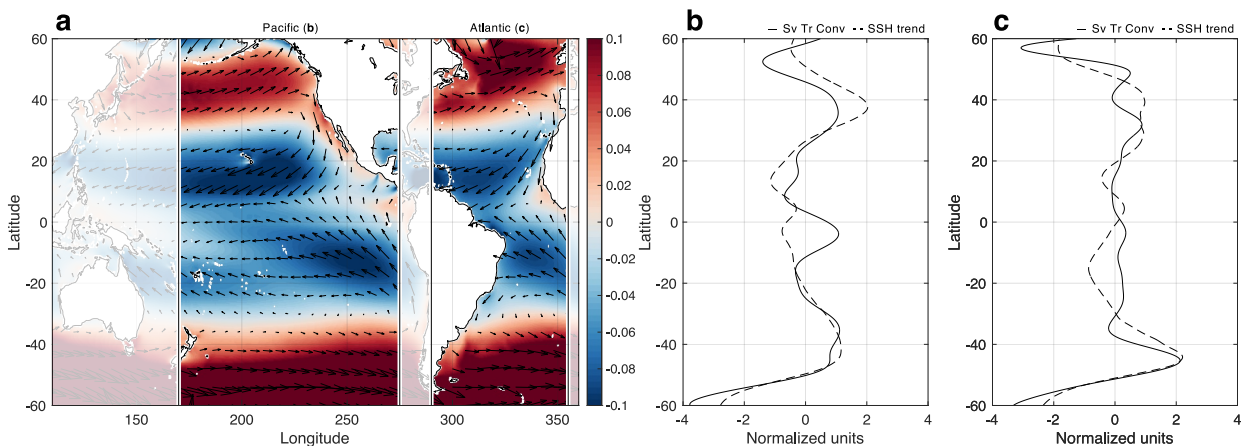


**Figure 4.** Latitudinal structure of sea level rise explained by Sverdrup dynamics. (a) Annual mean zonal wind stress ( $\text{N}/\text{m}^2$ ) and wind stress (arrows; skipping every 24 grid points for clarity), with lines along  $170^\circ\text{E}$ ,  $285^\circ\text{E}$ , and  $355^\circ\text{E}$  marking boundaries for Pacific and Atlantic calculations. (b) Latitudinal profiles of Pacific zonal mean SSH trend (dashed) and meridional convergence of Sverdrup transport  $\frac{\partial}{\partial y} \left( \frac{1}{\rho \beta} \frac{\partial \tau_x}{\partial y} \right)$  (solid); correlation 0.76. (c) As in panel (b) but for the Atlantic; correlation 0.81.

Regions of the Pacific and Atlantic not included in the Pacific and Atlantic zonal mean calculations are covered by semitransparent boxes. All profiles in panels (b and c) smoothed in latitude and plotted in normalized units (mean removed and scaled by standard deviation).

due to capturing the peaks in sea level rise around latitudes  $\pm 40^\circ$  (*i.e.*, near the poleward edges of the subtropical gyres). In the Atlantic, similar results are obtained, with a correlation of 0.81 between the trends in Sverdrup transport convergence and SSH (Figure 4c). This result indicates that the trend in surface wind stress and implied change in wind-driven ocean circulation is key to setting the patterns of sea level rise.

The relationship between the computed transport convergences and the gyres is clarified by examining the Sverdrup stream function, both as calculated from observed winds (Figures 5a and 5b) and simulated by a numerical ocean model (Figure 5c). The simulated gyre circulations in both the northern and southern subtropical Pacific Ocean systematically shift northward in response to the imposed forcing (wind stress trends). The highlighted area in the North Pacific (Figures 5b–5d) illustrates one regional example wherein due to the poleward-shifted gyres, the anomalous Sverdrup transports are converging upon a latitude at which a higher rate of sea level rise is observed in the altimeter record. While there are local extreme values within these broad stretches of accelerated sea level rise in the midlatitudes (discussed in the previous section), the essence of the pattern appearing prominently in each of the major ocean basins is explained rather well by this relatively straightforward metric of the wind's influence on the ocean.

### 3.3. Eastern Boundaries and the Tropical Pacific: The Ekman Perspective

A ubiquitous feature of the patterns of sea level rise in the Pacific—including the north, south, and tropical Pacific—is a basin-wide zonal gradient, wherein sea level is rising faster in the west and slower along the eastern boundaries (Figure 1e), which is also highly consistent with SST trends (Figures 1f and 1g). While Sverdrup dynamics are well suited to diagnosing meridional convergences and thus latitudinal gradients of SSH change, the mechanisms driving the large-scale zonal gradient thereof are primarily derived from Ekman dynamics—that is, the movement of the upper ocean strictly under the balance of wind stress and Earth's rotation. From the observed trends in wind stress curl over the altimeter-era, the Ekman pumping velocity can be calculated, which invokes continuity to diagnose vertical motion owing to the divergence of horizontal Ekman transports (upward for diverging Ekman transports and downward for converging Ekman transports). In the northeastern Pacific, the pattern of the wind stress trend is such that the upward Ekman pumping velocity along the West Coast of North America has increased by  $\sim 10$  m/day since 1993 (Figure 6a). The natural consequence of this upwelling trend is to lift the thermocline and cool SST (Figure 6c), which is clearly reflected in a lowering of SSH (relative to the global mean trend) along the same stretch of coastline from southern California to the Aleutian Islands (Figure 6b). Considering the consistency between SST trends beginning in 1993 and 1982, particularly the cooling (relative to the global mean trend) along the West Coast of North America (Figures 1f and 1h), it is expected that this relative lack of sea level rise has been ongoing since well before the altimeter record (and may

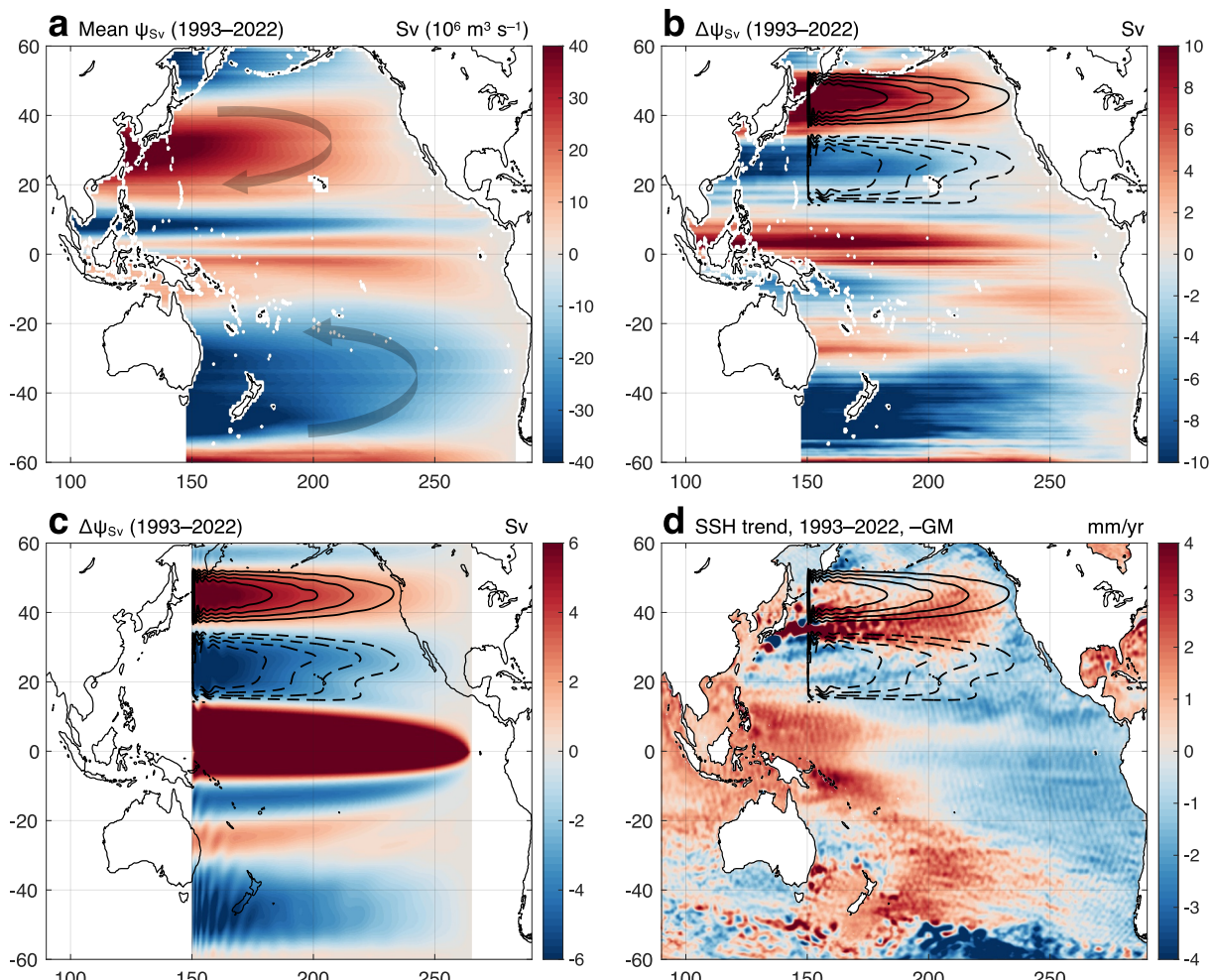


**Figure 5.** Midlatitude sea level rise maxima reflect poleward-shifting wind-driven gyres. (a) Annual mean Sverdrup stream function ( $\psi_{\text{Sv}}$ ) calculated from observed wind stress over 1993–2022 (Sv, or  $10^6 \text{ m}^3 \text{ s}^{-1}$ ). As annotated, the Sverdrup transport circulation is clockwise (counterclockwise) about positive (negative) values of  $\psi_{\text{Sv}}$ . (b) As in panel (a) but for the trend (Sv per 30 years). (c) As in panel (b) but for the trend simulated by the barotropic ocean model described in Section 2 forced by the observed Pacific zonal mean trend in zonal wind stress. (d) Observed linear trend in SSH from 1993 to 2022 (mm/yr) relative to the global mean (70°S–70°N, area-weighted). A set of four stream function contours from c is superimposed on b and d to indicate an exemplary region wherein the anomalous (or trend in) meridional convergence of Sverdrup transport corresponds to rates of sea level rise that are substantially higher than the global mean.

continue into the future). Indeed, analysis of tide gauge records along the U.S. West Coast by Merrifield (2011) reveals a flattening in the early 1980s of previously positive and significant sea level trends from San Diego to Seattle, where the timing of large decadal fluctuations appears to play an important role in such trends. As will be discussed below, this regional trend is also an emergent feature of global climate model simulations of the same time period.

Further from the North American coastline in the northeastern Pacific Ocean (central box in Figure 6), a series of persistent marine heat waves (MHW) have occurred since the mid-2010s, as clearly reflected in the SST trend since 1993 (Figure 6c). The first of such MHWs to be identified and studied extensively was the so-called “blob” of 2014–2015 (Bond et al., 2015), with myriad impacts on marine ecosystems and terrestrial hydroclimate (Holbrook et al., 2019; Shi et al., 2021). Several more MHWs in that location have since developed—including the recent “Blob 2.0” from 2019 to 2021. Compared to the dynamics of the negative relative SSH trend along the coast, attributable essentially to an increase in the upwelling-favorable, northerly alongshore winds (Figure 6a), the mechanisms of MHWs influencing the offshore SST trend appearing in Figure 6c are not straightforward, with an important role for not only reduced evaporative heat flux and cloud feedbacks (Amaya

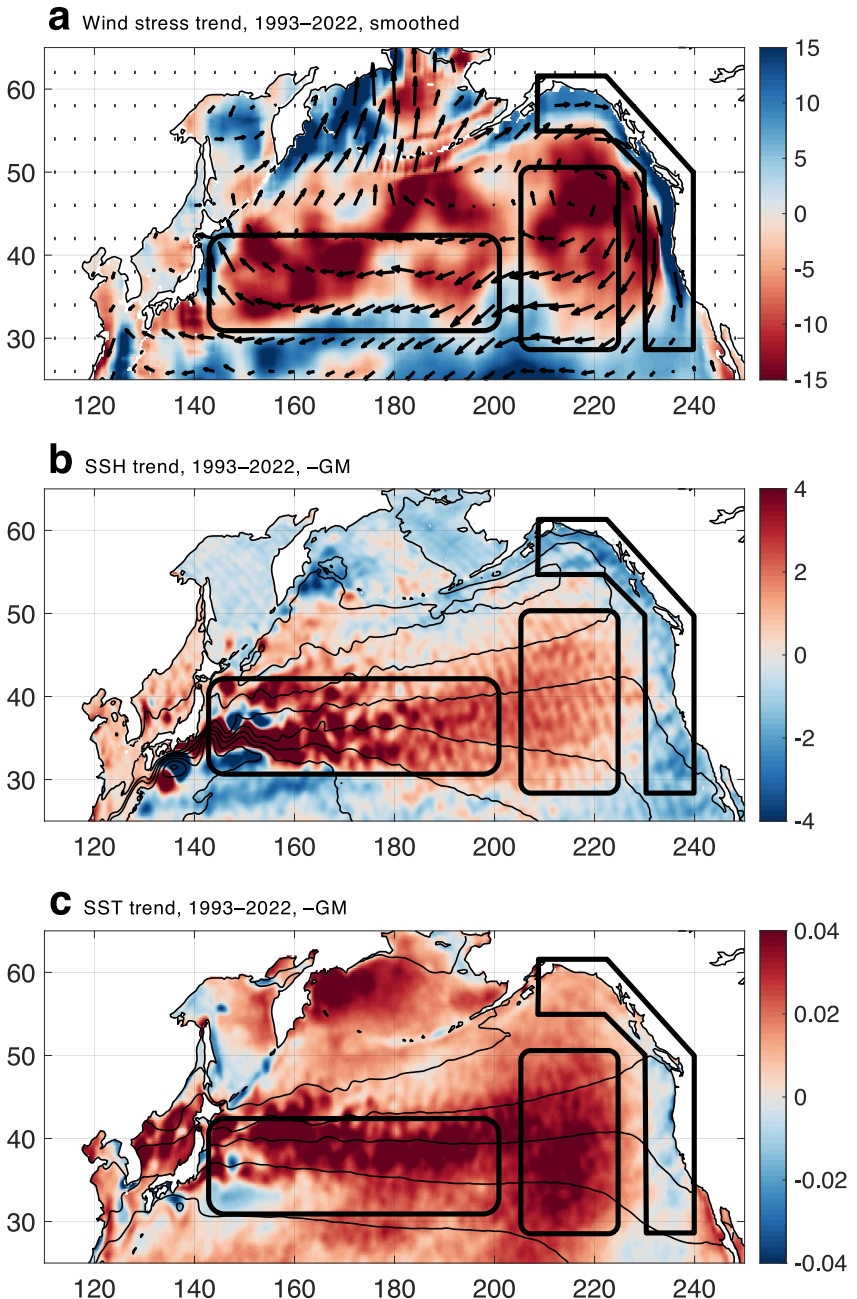


**Figure 6.** Ekman transport mitigates sea level rise along the West Coast of North America. (a) Observed trend in wind stress (arrows; skipping every 16 grid points for clarity) and Ekman pumping velocity (m/yr per 30 years; upward positive/blue) smoothed with a 4° latitude by longitude spatial filter and several regions identified as discussed in the main text. (b) As in (a) but for SSH (mm/yr) relative to the global mean (70°S–70°N, area-weighted) and not smoothed. (c) As in panel (b) but for sea surface temperature (°C/yr).

et al., 2020) but also interacting modes of climate variability (Joh & Di Lorenzo, 2017) and greenhouse gas forcing (Barkhordarian et al., 2022).

Given that Ekman dynamics played an insignificant role in the development of the recent string of MHWs in the northeastern Pacific (Figures 6a and 6c, and the aforementioned studies), and that surface heat fluxes were important, it is not clear what consequences such midlatitude MHWs would have for the regional SSH trend, other than to overwhelm the SST cooling along some parts of the coastline that would otherwise have occurred due to the Ekman pumping trend, and potentially to reinforce the anticyclonic wind anomaly that places northerly

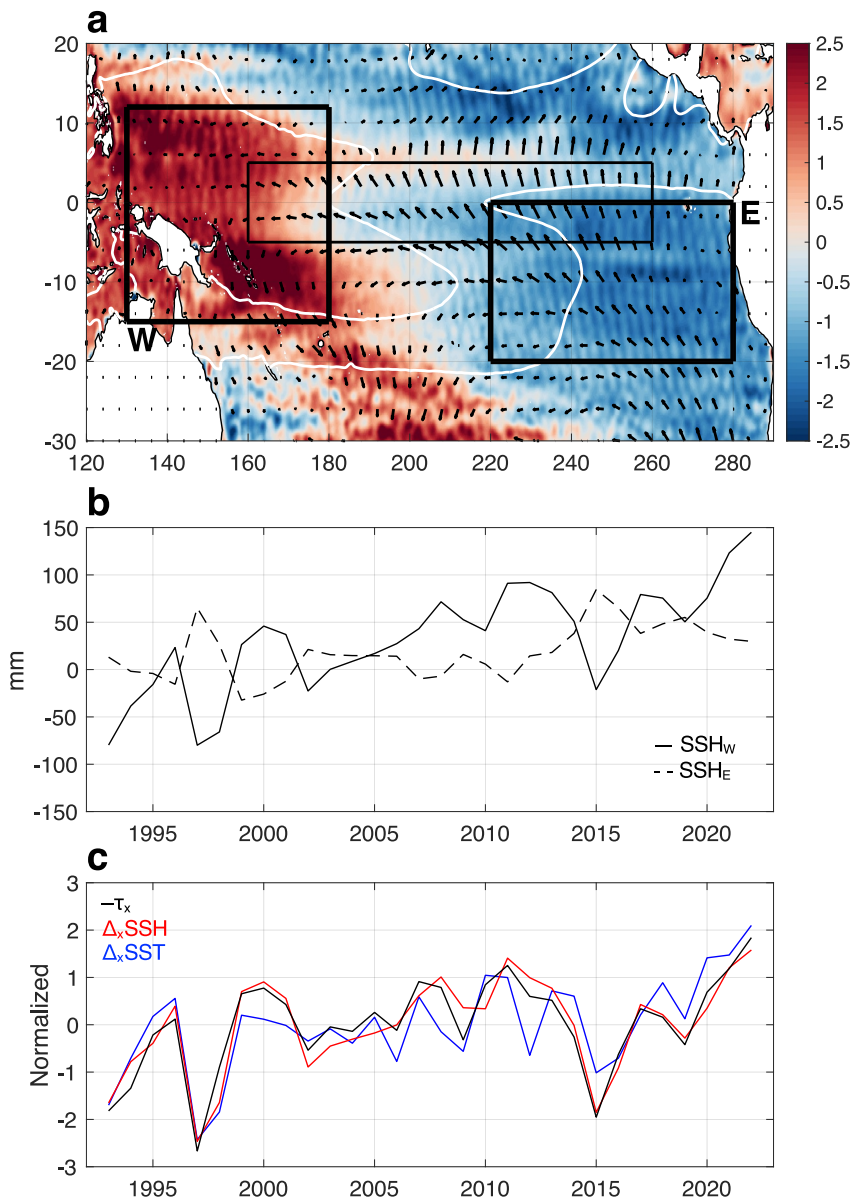


**Figure 7.** Zonal gradients in SSH and sea surface temperature (SST) coupled to easterly trade winds. (a) Observed linear trend in SSH from 1993 to 2022 (mm/yr) relative to the global mean ( $70^{\circ}\text{S}$ – $70^{\circ}\text{N}$ , area-weighted) with the  $26^{\circ}\text{C}$  and  $28.5^{\circ}\text{C}$  isotherms of the annual mean SST field (white contours), the trend in wind stress (arrows; skipping every 16 grid points for clarity) and regions identifying the western Pacific (W), eastern Pacific (E), and a central region (thin black box). (b) Time series of annual mean SSH in the western Pacific (solid) and eastern Pacific (dashed). Detrended correlation  $-0.91$ . (c) Time series of zonal wind stress in the central region (black; inverted for clarity), the zonal difference in SSH (red), and the zonal difference in SST (red; zonal differences taken as W minus E). Detrended correlation zonal SSH gradient versus inverted zonal wind stress  $0.94$ .

(upwelling-favorable) wind stress trends along the West Coast of North America. It is also possible that downward Ekman pumping diagnosed from wind stress trends in the west/central North Pacific (western box in Figure 6) contributed to the higher rates of sea level rise there, although there is substantial latitudinal offset between those features, but as discussed in the previous section, Sverdrup dynamics turns out to be a superior perspective to explain the pattern in that region.

Ekman dynamics is also an apt tool to understand the pattern of sea level rise within the tropical Pacific, particularly the stark zonal contrast in SSH trends (Figure 7a). The mean state of the tropical Pacific is

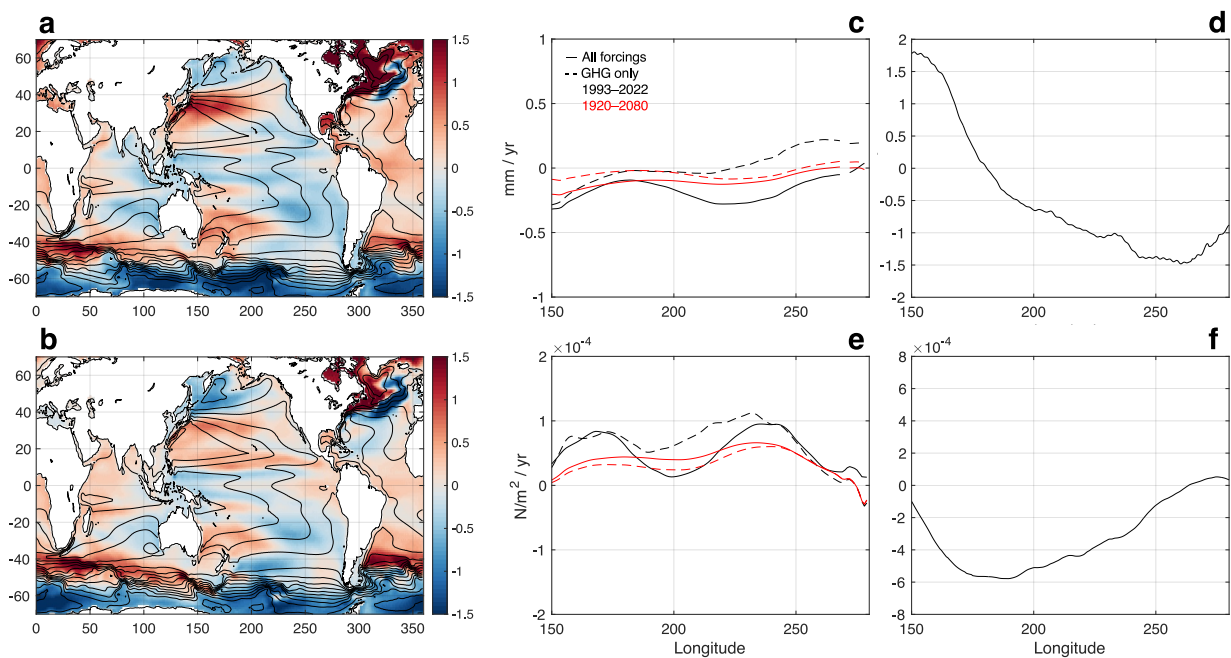


**Figure 8.** CESM1-simulated trends in SSH and easterly trades. (a) Ensemble mean SSH trend (mm/yr) from 1993 to 2022 simulated by CESM1 with all forcings (32 members). The model-simulated MDT field is contoured every 0.2 m. (b) As in panel (a) but for greenhouse gas forcing only (20 members). (c) Longitudinal profiles of sea surface temperature trends along the equatorial Pacific (averaged 2°S–2°N) from (a) (solid) and (b) (dashed) as well as the trends taken over the period 1920–2080 (red). (d) As in panel (c) but for the observed SSH trend in the equatorial Pacific over 1993–2022. (e and f) As in panels (c and d) but for zonal wind stress ( $N/m^2/yr$ ). Profiles based on observations (d and f) are smoothed with a 10° longitude filter.

characterized by zonal gradients in terms of temperature (thermocline depth and SST) as well as SSH. The thermocline depth, SST, and SSH decrease from the warm pool region in the west to the cold tongue in the east, held in a quasi-equilibrium by the easterly trade winds that is interrupted periodically by El Niño and La Niña events. The trend in SSH over the altimeter-era projects very strongly onto the mean patterns of SSH and SST (marked by white contours on Figure 7a), signifying an intensification of the mean gradients. Naturally, this is accompanied by an observed strengthening of the trade wind regime over the tropical Pacific—not only the zonal component along the equator, but also the southeasterlies in the eastern Pacific (Figure 7a).

One cannot simply conclude from the above result that the SSH gradient has strengthened since 1993 because the trade winds have; the atmosphere and ocean are tightly coupled in this region through the Bjerknes (1969) feedback. For example, if there exists a mechanism by which the ocean surface warms more slowly (or even cools) in the eastern Pacific in response to external forcing (e.g., Clement et al., 1996; Heede & Fedorov, 2021), then the trade winds will respond by strengthening according to Lindzen and Nigam (1987), which will amplify the zonal tilt of the thermocline and further amplify the change in the zonal SST and SSH gradients. This robust coupling across timescales can be seen through the coevolution of SSH in the western and eastern Pacific (Figure 7b), and that of the zonal SSH and SST gradients with the strength of the easterly trade winds along the equator (Figure 7c). Over the altimeter record, SSH in the western and eastern Pacific have fluctuated out of phase due to ENSO (detrended correlation  $-0.91$ ), and their trends are divergent (with negligible sea level rise in the eastern tropical Pacific). The coupling with the easterly trade winds is also remarkably tight, being correlated to the zonal SSH gradient at  $r = 0.94$  after detrending, and both are trending stronger since 1993. As will be discussed in the following section, there is a stark disagreement in the tropical Pacific between observations and ensembles of global climate model simulations driven by historical radiative forcings.

### 3.4. The Climate Model Perspective

Comparing the regional patterns of sea level rise from the altimeter record with those of the ensemble mean of the CESM1 and CESM2 over the same 30-year time period (Figures 8a and 9a) reveals striking consistency in terms of many of the large-scale features discussed above. These include the maxima that are spread across the

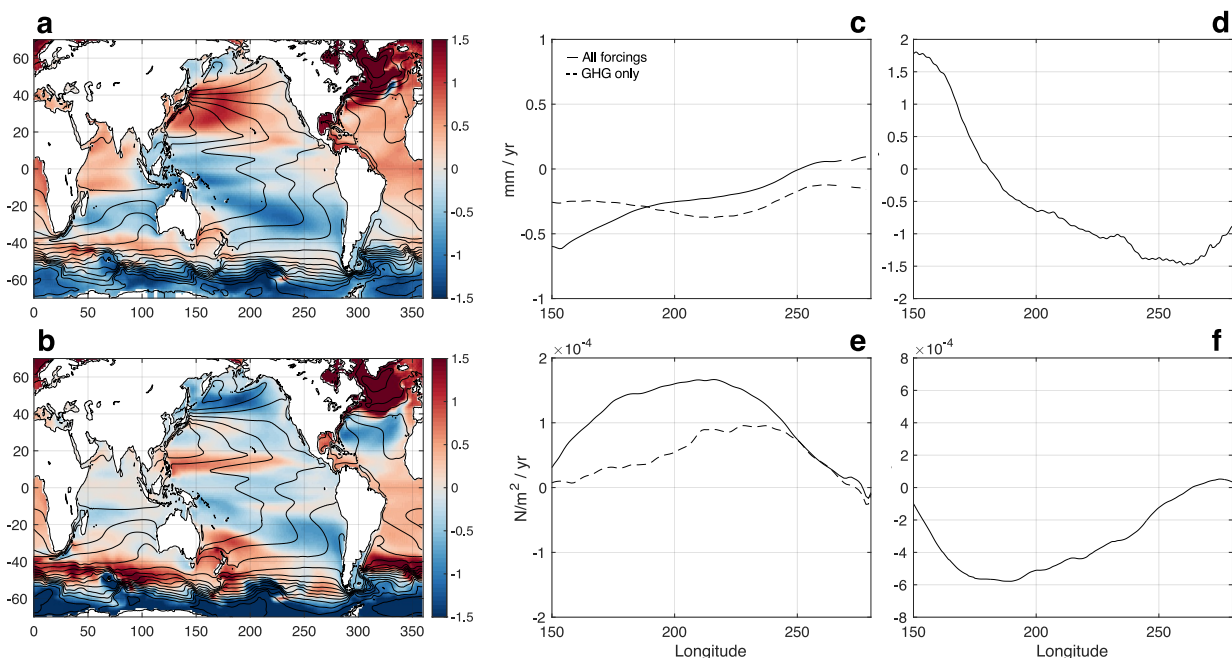


**Figure 9.** CESM2-simulated trends in SSH and easterly trades. As in Figure 8 but for CESM2.

midlatitudes (around  $\pm 40^\circ$ ) due to poleward-shifting subtropical gyres and zones of Sverdrup transport convergence, the minimum in the Southern Ocean along the sharp gradient in MDT, the eastern boundary coastal minima due to Ekman pumping trends, and other prominent features not discussed in detail here such as the maximum in the southwestern tropical Indian Ocean and the minimum in the high-latitude North Atlantic. As these are the averages of dozens of ensemble members with different realizations of internal variability, the presence of those observed features in this model experiment (and other ensembles, e.g., Yang et al., 2020) suggests they are at least partially driven by external (radiative) forcing rather than purely an expression of internal climate variability (Fasullo & Nerem, 2018). All of those features are also present in the greenhouse gas-only single-forcing ensemble mean (Figures 8b and 9b), with the exception of the eastern boundary coastal minima—those only emerge in the single-forcing ensemble means that include aerosols (industrial and biomass, not shown).

The notable exception to the aforementioned global consistency between the altimeter record and the CESM large ensembles since 1993 is, rather fittingly, the tropical Pacific. This conspicuous mismatch, in which the altimeter trend portrays a strengthening zonal SSH gradient and the model simulates a weakening zonal SSH gradient (Figures 8c, 8d, 9c, and 9d), is symptomatic of a wholesale mismatch of trends within the tropical Pacific involving all of the other variables of the coupled system to which the SSH field is linked including SST and sea level pressure (Wills et al., 2022). In particular, the easterly trade winds over the equatorial Pacific strengthened substantially over this period in the real world (Figure 8f), whereas both CESM large ensembles simulate a weakening of the trades—a mere continuation of a trend that runs through the entirety of those historical simulations beginning in 1920 (in CESM1—Figure 8e). This discrepancy extends into the tropical Indian Ocean—in particular, the zonal contrast of SSH trends there. In both observations and CESM ensembles, the eastern Indian Ocean tends to change with the western Pacific (as a so-called Indo-Pacific Warm Pool [IPWP]), and a Bjerknes-like feedback involving the zonal wind response leads to a gradient in SSH change extending westward where the sign ultimately changes from that found in the eastern tropical Indian Ocean.

How much *could* we expect the observed pattern of sea level rise to match that simulated by a global climate model over a 30-year period like 1993–2022, especially given the presence of internal climate variability? This can be assessed simply by quantifying the match between each individual member of a Large Ensemble and the ensemble mean, and then comparing that distribution with the observed match. For CESM1, the average percentage of the global ocean surface over which an individual member of the ensemble agrees on the sign of the trend with the ensemble mean (after removing the global mean of each) is approximately 70%, with a standard

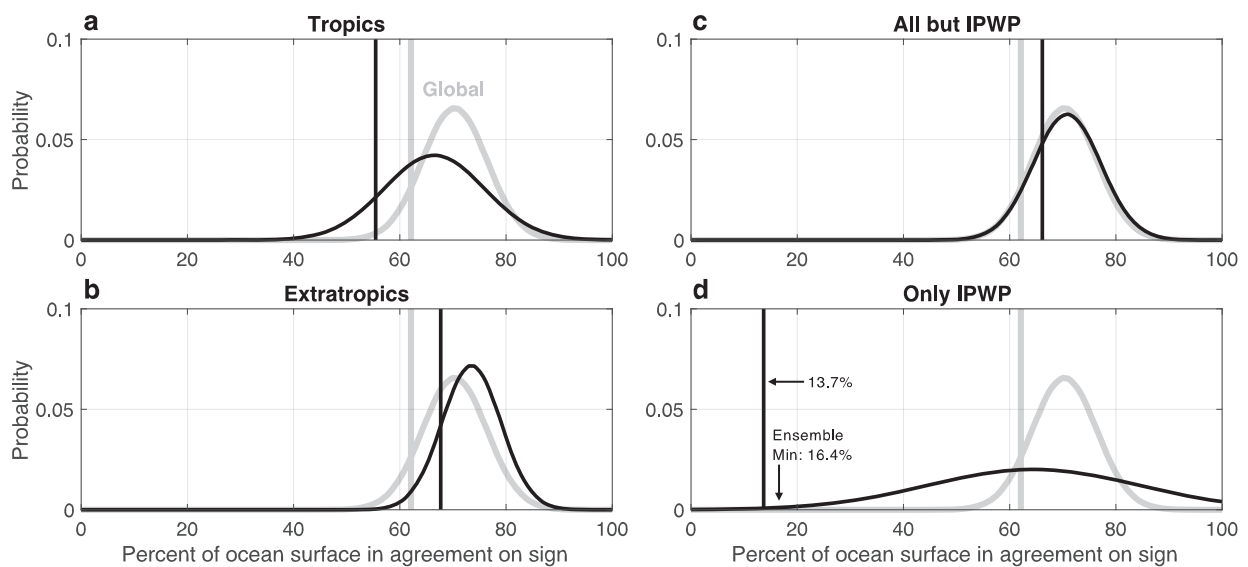


**Figure 10.** Diversity of sea level rise patterns within the CESM1 large ensemble. Probability distribution functions (PDFs) of the percent of the ocean surface in agreement on the sign of the SSH trend from 1993 to 2022 (mm/yr) relative to the global mean ( $70^{\circ}\text{S}$ – $70^{\circ}\text{N}$ , area-weighted) between each member of the CESM1 Large Ensemble and the ensemble mean for (a) the global tropics (within  $24^{\circ}$  of the equator), (b) the global extratropics (beyond  $24^{\circ}$  of the equator), (c) everywhere but the Indo-Pacific Warm Pool (IPWP), and (d) only the IPWP. The IPWP is defined as  $10^{\circ}\text{S}$ – $10^{\circ}\text{N}$   $\times$   $70^{\circ}\text{E}$ – $170^{\circ}\text{W}$ . Black vertical lines in each panel indicate the percent of the ocean surface in agreement on the sign of the SSH trend between the ensemble mean and observations for the geographic subdomain. In each panel, the gray PDF is for the global domain, and the gray vertical line indicates the percent of the global ocean surface in agreement on the sign of the SSH trend between the CESM1 ensemble mean and observations. The gray features are identical in each panel to facilitate comparison between each geographic subdomain and the global domain.

deviation of about 6% (Figure 10). The match between the ensemble mean and the observed trend is about 62%—well within the distribution. As shown in Figures 10b–10d, the greatest uniformity of trends among the ensemble members—and between the observations and the ensemble mean—is found in the extratropics. The match is lower for the tropics, largely due to the stark mismatch in the IPWP region. Results for the CESM2 Large Ensemble are similar (Figure 11). The average match between ensemble members and the ensemble mean is 74% for the global domain with a 5% standard deviation, and the extratropics exhibits the strongest uniformity of trends and match with observations. However, the overall match between the CESM2 ensemble mean and the observed trend is lower (53%).

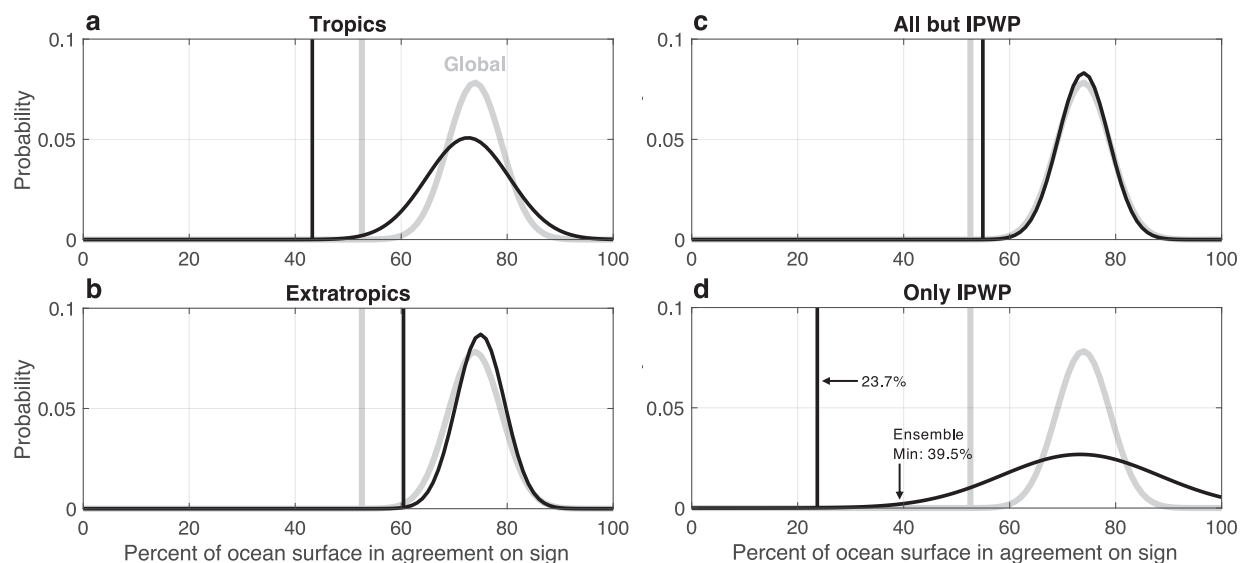


**Figure 11.** Diversity of sea level rise patterns within the CESM2 large ensemble. As in Figure 10 but for CESM2.

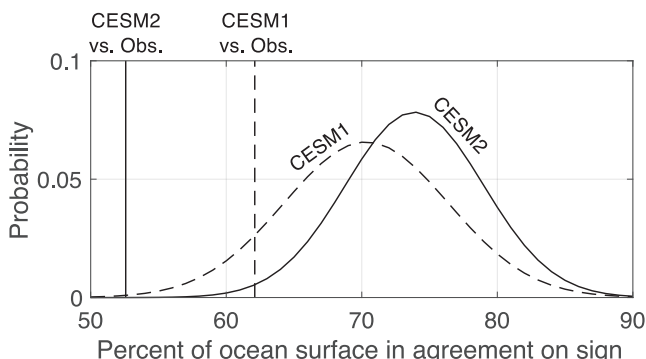


**Figure 12.** Diversity and agreement with observations from CESM1 to CESM2. Probability distribution functions (PDF) of the percent of the ocean surface in agreement on the sign of the SSH trend from 1993 to 2022 ( $\text{mm}/\text{yr}$ ) relative to the global mean ( $70^\circ\text{S}$ – $70^\circ\text{N}$ , area-weighted) between each member of the CESM1 (dashed) and CESM2 (solid) Large ensembles and the respective ensemble mean for the global domain. Vertical lines indicate the percent of the ocean surface in agreement on the sign of the SSH trend between the ensemble means and observations. Effectively plotted are the gray features from Figures 10 and 11 so that the two generations of CESM maybe compared directly.

Relative to CESM1, the CESM2 Large Ensemble has higher uniformity of trend patterns among ensemble members (distribution narrower and shifted toward higher percentages), and a lower match with the observed trend (Figure 12). While it is reasonable to conclude from the CESM1 Large Ensemble that the observed pattern of sea level rise from 1993 to 2022 could have been a realization selected from an ensemble of realizations whose mean is that of the CESM1 large ensemble, one cannot make such a conclusion based on CESM2. In fact, there is not a single member of the CESM2 Large Ensemble whose match with the ensemble mean is as low as the match between the observations and the CESM2 ensemble mean. Simply excluding the tropics or the IPWP does not alleviate said mismatch (Figure 11). One potential reason for the fact that CESM-simulated SSH trends “appear” (visually) strikingly similar to the altimeter record, and yet the fraction of the global ocean where the ensemble mean and observations agree on the sign of change (relative to the global mean trend) is surprisingly lower (particularly CESM2) than individual ensemble members, is related to mean state biases in key features of the ocean circulation such as gyres and western boundary currents. If models predict slightly offset changes in space (e.g., a gyre located too far poleward or a western boundary current positioned too far off the coast), then lower values of objective metrics quantifying their match will result.

The mismatch in the zonal structure of SSH (and SST) trends in the tropical Pacific between observations and models, and indeed the uncertainty in the future projections thereof, have consequences for sea level rise patterns outside of the tropical Pacific. The details of the pattern of heating (of the lower troposphere) within the tropical

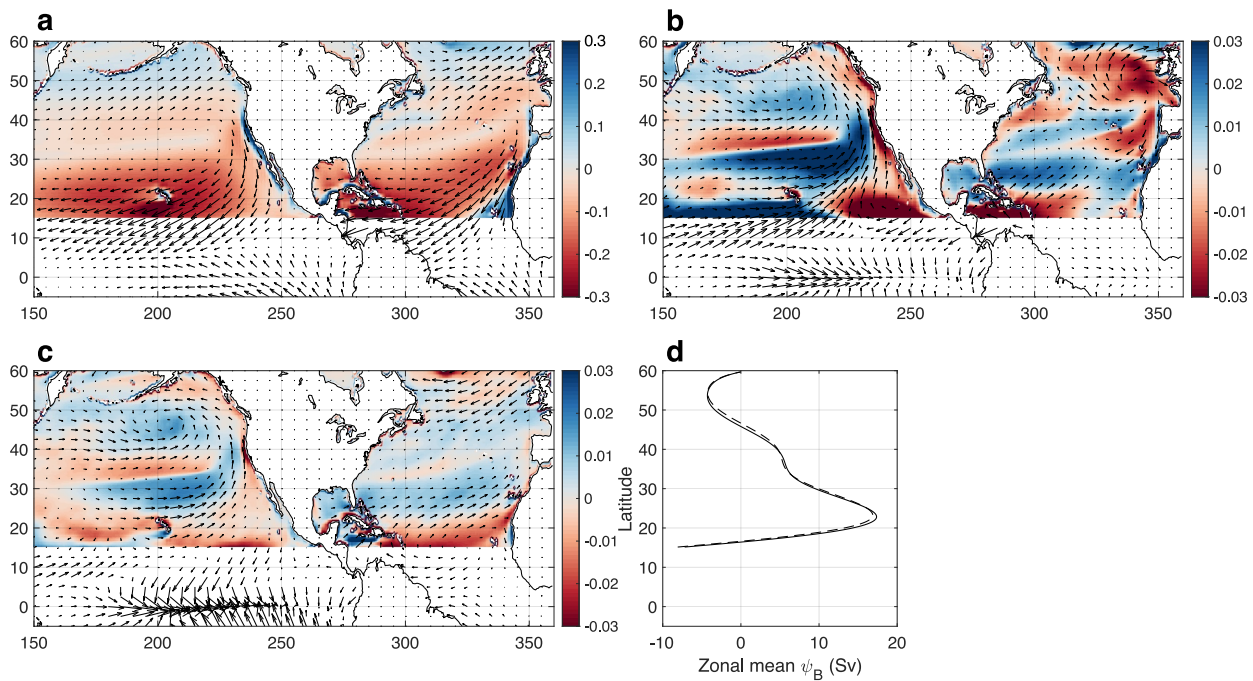


**Figure 13.** Impact of eastern Pacific warming on extratropical wind forcing. (a) Present-day Ekman pumping velocity (colors,  $\text{m}/\text{day}$ ) and surface wind stress (vectors,  $\text{N}/\text{m}^2$ ) in the North Pacific and Atlantic simulated by the CESM2-CAM6 global atmospheric model (EP experiment, averaged 2015–2034). Note that positive values (for upwelling) are indicated by blue colors. (b) Change in wind stress and Ekman pumping velocity simulated by CESM2-CAM6; EP experiment 2080–2099 relative to 2015–2034. (c) Difference in end-of-century (averaged 2080–2099) wind stress and Ekman pumping velocity between the EP and noEP experiments; the difference indicates the response to enhanced sea surface temperature warming in the eastern equatorial Pacific. Values of Ekman pumping velocity within  $15^\circ$  of the equator are masked because  $1/f \rightarrow \infty$  as  $\text{latitude} \rightarrow 0$ . (d) Pacific zonal mean stream function simulated by the barotropic ocean model described in Section 2, forced by the end-of-century Pacific zonal mean zonal wind stress in the EP (solid) and noEP (dashed) experiments.

Pacific can impact hemispheric-scale circulation via atmospheric Rossby and Kelvin wave adjustments, a concern noted recently by those studying future changes in Atlantic tropical cyclones (Karnauskas et al., 2023; Sobel et al., 2023), terrestrial hydroclimate (Alessi & Rugenstein, 2024), and much more (Rugenstein et al., 2023). Spatial derivatives and integrals of those remote surface wind patterns ultimately constrain gyres and upwelling systems à la Ekman and Sverdrup relations. This can be demonstrated by forcing an atmosphere-only version of CESM2 with SST trends that include—and exclude—the enhanced warming in the eastern equatorial Pacific (as in Karnauskas et al., 2023), and then interpreting its output from the perspective of wind-driven ocean dynamics.

Using the northern extratropical Pacific and Atlantic as an example, the CESM2-CAM6 model simulates a realistic present-day wind stress and Ekman pumping velocity distribution, including the climatological subtropical anticyclones driving gyre circulations and alongshore winds that in turn drive upwelling along the continental west coasts (Figure 13a). In response to the full SST change driven by anthropogenic forcing simulated by the *coupled* version of CESM2, there is an overall weakening of the North Pacific subtropical high including a weakening of the alongshore winds adjacent to North America (Figure 13b). What is the role of the enhanced SST warming in the eastern tropical Pacific simulated by this model, which is of course tied to the simulated zonal gradient of SSH? By contrasting the above result with an alternative experiment in which the enhanced eastern Pacific warming was removed from the SST forcing seen by the CESM2-CAM6, we see that the positive zonal gradient of SST warming is a first-order contributor to the weakening subtropical high and coastal upwelling (Figure 13c). Moreover, the impact of the enhanced eastern Pacific warming on the broader spatial pattern of wind stress curl is predicted by the barotropic ocean model (described previously) to drive a relatively minor strengthening (by ~3%) and equatorward shift (by ~1°) of the subtropical gyre (Figure 13d). Similar, but larger in magnitude, changes are also predicted for the southern Pacific subtropical gyre in this experiment (not shown).

From the classic view of coupled tropical dynamics and the Bjerknes feedback, the mismatch in the zonal structure of the SSH trends between observations and both the CESM1 and CESM2 is not surprising. This is indeed a relatively narrow view of a very big problem that transcends the science of sea level rise (Coats & Karnauskas, 2017; Seager et al., 2022; Lee et al., 2022). Given how sea level can be an integrator of climate signals by reflecting accumulations of mass and heat that occur through myriad steric and dynamic processes, closer collaborations between the fields could expedite progress. The results presented above also suggest that resolving the mismatch in the tropical Pacific is key to understanding extratropical patterns of sea level rise including such outstanding questions as the fate of the subtropical gyres and associated western boundary current systems, and why and for how long the West Coast of the U.S. will experience lower rates of sea level rise.

#### 4. Summary and Discussion

This paper has presented a wide-ranging analysis of regional sea level changes since 1993, as measured by satellite altimeters. These regional variations are found to be influenced by a complex mix of internal climate dynamics and external climate forcings. A notable aspect of this research is the application of a common diagnostic framework to synthesize these regional patterns across the global ocean. The study leverages a combination of oceanic and atmospheric observations with ensembles of advanced global climate models. A key finding is the pivotal role of wind forcing in shaping these patterns. The dynamics of Ekman and Sverdrup, in particular, have been instrumental in reproducing the large-scale structure of sea level change from the tropics to higher latitudes. Our main findings are as follows:

- The most significant local sea level changes occur in areas with sharp mean sea surface height gradients, where even small shifts in ocean circulation features can produce dramatic local effects.
- Sverdrup balance, fundamental in understanding wind-driven ocean circulation, reveals that changes in global atmospheric circulation and wind stress are crucial in determining the latitudinal structure of sea level rise, as evidenced by the strong correlation between trends in Sverdrup transport convergence and sea level changes.
- The global pattern of sea level rise, characterized by faster rates in the west and slower along eastern boundaries, aligns with SST trends and is primarily driven by Ekman dynamics, which explain both the increased upwelling along the West Coast of North America and the complex interplay of marine heat waves and wind stress trends in the northeastern Pacific.
- In the tropical Pacific, Ekman dynamics reveal an intensification of zonal contrasts in sea level rise, with strengthening trade winds amplifying these gradients, although determining whether these trends are a

response to anthropogenic forcing remains challenging given the limited altimeter data and discrepancies with climate model simulations.

- A comparison between the regional patterns of sea level rise observed from altimeter data and those simulated by large ensembles of global climate models reveals some consistency, which is dependent on model version.

The latter findings indicate that some observed features are at least partially driven by external radiative forcing rather than internal climate variability, except for a significant mismatch in the tropical Pacific, where the model's weakening zonal SSH gradient contrasts with the observed strengthening, reflecting broader challenges in understanding coupled tropical dynamics and the need for interdisciplinary collaboration.

From the perspective of the altimeter record, we are considering a shorter period of time for a region with such large interannual and decadal variability (marked by ENSO and Pacific decadal variability). There is a vast literature studying the historical (and future) evolution of these zonal gradients in the tropical Pacific using instrumental records and climate models (see Capotondi et al. (2023) and Lee et al. (2022) for recent reviews), and perhaps due to the length of the record, fewer have embraced the perspective of SSH—a rather precise measurement that is also diagnostic of crucial features of the coupled system such as the thermocline depth. The question of whether the observed SSH trend in the tropical Pacific is primarily a response to anthropogenic forcing maybe impossible to answer using measurements since 1993. It is worth pointing out that the SST trend in the tropical Pacific over the altimeter record, which is tightly coupled to that of SSH (Figure 7c), is similar when considering the full satellite record of SST back to 1982 (Figures 1f and 1h), and that instrumental records extending back into the nineteenth century also indicate a long-term strengthening of the zonal SST gradient (Karnauskas et al., 2009; Lee et al., 2022; Seager et al., 2022).

We acknowledge that none of the models analyzed herein include the barystatic component of sea level change. The absence of this geophysical process in our models could lead to slight discrepancies in our predictions for specific regions, especially those influenced by nearby ice sheets. Incorporating barystatic sea level change caused by the present-day GRD effects from ice mass loss could refine our model's ability to simulate the nuances of sea level changes linked to ice mass loss. This integration would enable more accurate assessments of regional sea level changes, particularly in high-latitude regions where the redistribution of ocean mass due to GRD effects plays a prominent role (Adhikari et al., 2016; Coulson et al., 2022). However, we do not expect this advancement would significantly alter the main conclusions of the present work. We have shown that while the barystatic component of sea level rise is significant in terms of the global mean rate, it does not substantially modify the pattern of total sea level change in the regions considered, which is primarily driven by sterodynamics (Figure 2).

This paper highlights the importance of these observed regional variations in sea level rise, not only for their societal impacts, especially along coastlines but also for their significance in understanding the dynamics of global ocean circulation. Looking forward, we emphasize the challenges in predicting future sea level changes, primarily due to the difficulties in distinguishing between natural variability and human-induced changes. By using satellite altimeter observations of sea level over the last 30 years to better understand the coupled ocean and atmospheric dynamics that drive ocean heat transport, we can improve climate model projections of future sea level rise, but we can also use that knowledge to better design more data-driven sea level projections, including projections that utilize artificial intelligence including machine learning. These insights will only get more informative as the observational record lengthens. This issue is critical for understanding the “hotspots” of accelerated sea level rise and underscores the necessity for region-specific studies. Such research is essential to enhance our understanding of the interplay between natural and anthropogenic factors driving regional sea level changes. Improved knowledge in this area is vital for developing more accurate predictions and formulating effective adaptation strategies for future sea level scenarios.

## Conflict of Interest

The authors declare no conflicts of interest relevant to this study.

## Data Availability Statement

Add data sets used in this study, observations, and model outputs alike, are freely and publicly available. Following is a list of DOIs or URLs (if *data* DOIs are not available) for each data set used in this study. Jet

Propulsion Laboratory SSH (<https://doi.org/10.5067/SLREF-CDRV3>); CMEMS SSH (<https://doi.org/10.48670/moi-00148>); AVISO MDT (<https://doi.org/10.24400/527896/a01-2023.003>); NOAA OIv2 SST (<https://psl.noaa.gov/data/gridded/data.noaa.oisst.v2.highres.html>); ERA5 wind stress (<https://doi.org/10.24381/cds.f17050d7>); CESM1 LE (<https://www.cesm.ucar.edu/community-projects/lens>); CESM1 SF (<https://www.cesm.ucar.edu/working-groups/climate/simulations/cesm1-single-forcing-le>); CESM2 LE (<https://www.cesm.ucar.edu/community-projects/lens2>); CESM2 SF (<https://www.cesm.ucar.edu/working-groups/climate/simulations/cesm2-single-forcing-le>); and CESM2-CAM6 (<https://doi.org/10.5281/zenodo.8157139>).

## Acknowledgments

The authors acknowledge support from the NASA Sea Level Change program (80NSSC20K1123 for KBK and RSN), and thank Mike Grissom for sharing MATLAB code for the barotropic ocean model. The efforts of Dr. Fasullo in this work were supported by NASA Awards 80NSSC21K1191, 80NSSC17K0565, and 80NSSC22K0046, and by the Regional and Global Model Analysis (RGMA) component of the Earth and Environmental System Modeling Program of the U.S. Department of Energy's Office of Biological & Environmental Research (BER) under Award Number DE-SC0022070. Dr. Fasullo was also supported by NSF Award 2103843. NASA Sea Level Change program award for KBK and RSN: 80NSSC25K7226.

## References

- A, G., Wahr, J., & Zhong, S. (2013). Computations of the viscoelastic response of a 3-D compressible Earth to surface loading: An application to Glacial Isostatic Adjustment in Antarctica and Canada. *Geophysical Journal International*, 192(2), 557–572. <https://doi.org/10.1093/gji/ggs030>
- Adhikari, S., Ivins, E. R., & Larour, E. (2016). ISSM-SESAW v1.0: Mesh-based computation of gravitationally consistent sea-level and geodetic signatures caused by cryosphere and climate driven mass change. *Geoscientific Model Development*, 9(3), 1087–1109. <https://doi.org/10.5194/gmd-9-1087-2016>
- Alessi, M. J., & Rugenstein, M. (2024). Potential near-term wetting of the Southwestern United States if the Eastern and Central Pacific cooling trend reverses. *Geophysical Research Letters*, 51(13), e2024GL108292. <https://doi.org/10.1029/2024GL108292>
- Amaya, D. J., Miller, A. J., Xie, S.-P., & Kosaka, Y. (2020). Physical drivers of the summer 2019 north pacific marine heatwave. *Nature Communications*, 11, 1–9. <https://doi.org/10.1038/s41467-020-15820-w>
- Bamber, J. L., & Riva, R. E. M. (2010). The sea level fingerprint of recent ice mass fluxes. *The Cryosphere*, 4, 621–627. <https://doi.org/10.5194/tc-4-621-2010>
- Barkhordarian, A., Nielsen, D. M., & Baehr, J. (2022). Recent marine heatwaves in the North Pacific warming pool can be attributed to rising atmospheric levels of greenhouse gases. *Communications Earth & Environment*, 3(1), 131. <https://doi.org/10.1038/s43247-022-00461-2>
- Bartholeit, A., Milne, G. A., & Latychev, K. (2021). Modelling sea-level fingerprints of glaciated regions with low mantle viscosity. *Earth System Dynamics*, 12(3), 783–795. <https://doi.org/10.5194/esd-12-783-2021>
- Bjerknes, J. (1969). Atmospheric teleconnections from the equatorial Pacific. *Monthly Weather Review*, 97(3), 163–172. [https://doi.org/10.1175/1520-0493\(1969\)097<0163:attep>2.3.co;2](https://doi.org/10.1175/1520-0493(1969)097<0163:attep>2.3.co;2)
- Bond, N. A., Cronin, M. F., Freeland, H., & Mantua, N. (2015). Causes and impacts of the 2014 warm anomaly in the NE pacific. *Geophysical Research Letters*, 42(9), 3414–3420. <https://doi.org/10.1002/2015gl063306>
- Bronsema, B., & Zanna, L. (2020). Heat and carbon coupling reveals ocean warming due to circulation changes. *Nature*, 584(7820), 227–233. <https://doi.org/10.1038/s41586-020-2573-5>
- Camargo, C. M. L., Riva, R. E. M., Hermans, T. H. J., & Slanger, A. B. A. (2022). Trends and uncertainties of mass-driven sea-level change in the satellite altimetry era. *Earth System Dynamics*, 13(3), 1351–1375. <https://doi.org/10.5194/esd-13-1351-2022>
- Capotondi, A., McGregor, S., McPhaden, M. J., Cravatte, S., Holbrook, N. J., Imada, Y., et al. (2023). Mechanisms of tropical Pacific decadal variability. *Nature Reviews Earth & Environment*, 4(11), 754–769. <https://doi.org/10.1038/s43017-023-00486-x>
- Clark, J. A., & Lingle, C. S. (1977). Future sea-level changes due to West Antarctic ice sheet fluctuations. *Nature*, 269(5625), 206–209. <https://doi.org/10.1038/269206a0>
- Clement, A. C., Seager, R., Cane, M. A., & Zebiak, S. E. (1996). An ocean dynamical thermostat. *Journal of Climate*, 9, 2190–2196. [https://doi.org/10.1175/1520-0442\(1996\)009<2190:aodt>2.0.co;2](https://doi.org/10.1175/1520-0442(1996)009<2190:aodt>2.0.co;2)
- Coats, S., & Karnauskas, K. B. (2018). A role for the Equatorial Undercurrent in the ocean dynamical thermostat. *Journal of Climate*, 31(16), 6245–6261. <https://doi.org/10.1175/JCLI-D-17-0513.1>
- Conrad, C. P., & Hager, B. H. (1997). Spatial variations in the rate of sea level rise caused by the present-day melting of glaciers and ice sheets. *Geophysical Research Letters*, 24(12), 1503–1506. <https://doi.org/10.1029/97gl01338>
- Copernicus Marine Environment Monitoring Service (CMEMS). (2023). Global Ocean Gridded L4 Sea Surface heights and derived variables reprocessed 1993 ongoing. <https://doi.org/10.48670/moi-00148>
- Coulson, S., Dangendorf, S., Mitrovica, J. X., Tamisiea, M. E., Pan, L., & Sandwell, D. T. (2022). A detection of the sea level fingerprint of Greenland Ice Sheet melt. *Science*, 377, 1550–1554. <https://doi.org/10.1126/science.abo0926>
- Danabasoglu, G., Lamarque, J.-F., Bacmeister, J., Bailey, D. A., DuVivier, A. K., Edwards, J., et al. (2020). The Community Earth System Model Version 2 (CESM2). *Journal of Advances in Modeling Earth Systems*, 12, e2019MS001916. <https://doi.org/10.1029/2019MS001916>
- Dangendorf, S., Hendricks, N., Sun, Q., Klinck, J., Ezer, T., Frederikse, T., et al. (2023). Acceleration of U.S. Southeast and Gulf coast sea-level rise amplified by internal climate variability. *Nature Communications*, 14(1), 1935. <https://doi.org/10.1038/s41467-023-37649-9>
- Deser, C., Phillips, A. S., Simpson, I. R., Rosenbloom, N., Coleman, D., Lehner, F., et al. (2020). Isolating the evolving contributions of anthropogenic aerosols and greenhouse gases: A new CESM1 large ensemble community resource. *Journal of Climate*, 33(18), 7835–7858. <https://doi.org/10.1175/JCLI-D-20-0123.1>
- Domingues, R., Goni, G., Baringer, M., & Volkov, D. (2018). What caused the accelerated sea level changes along the U.S. East Coast during 2010–2015? *Geophysical Research Letters*, 45(24), 13367–13376. <https://doi.org/10.1029/2018GL081183>
- Dong, S., Sprintall, J., & Gillie, S. T. (2006). Location of the Antarctic polar front from AMSR-E satellite Sea Surface temperature measurements. *Journal of Physical Oceanography*, 36(11), 2075–2089. <https://doi.org/10.1175/jpo2973.1>
- Ezer, T. (2019). Regional differences in sea level rise between the Mid-Atlantic Bight and the South Atlantic Bight: Is the Gulf Stream to blame? *Earth's Future*, 7, 771–783. <https://doi.org/10.1029/2019EF001174>
- Fasullo, J. T., & Gent, P. R. (2017). On the relationship between regional ocean heat content and Sea Surface height. *Journal of Climate*, 30(22), 9195–9211. <https://doi.org/10.1175/jcli-d-16-0920.1>
- Fasullo, J. T., & Nerem, R. S. (2018). Altimeter-era emergence of the patterns of forced sea-level rise in climate models and implications for the future. *Proceedings of the National Academy of Sciences of the United States of America*, 115(51), 12944–12949. <https://doi.org/10.1073/pnas.1813233115>
- Fasullo, J. T., Gent, P. R., & Nerem, R. S. (2020a). Forced patterns of sea level rise in the community Earth system model large ensemble from 1920 to 2100. *Journal of Geophysical Research: Oceans*, 125(6), e2019JC016030. <https://doi.org/10.1029/2019JC016030>

- Fasullo, J. T., Gent, P. R., & Nerem, R. S. (2020b). Sea level rise in the CESM large ensemble: The role of individual climate forcings and consequences for the coming decades. *Journal of Climate*, 33(16), 6911–6927. <https://doi.org/10.1175/JCLI-D-19-1001.1>
- Fasullo, J. T., Lamarque, J.-F., Hannay, C., Rosenbloom, N., Tilmes, S., DeRepentigny, P., et al. (2022). Spurious late historical-era warming in CESM2 driven by prescribed biomass burning emissions. *Geophysical Research Letters*, 49(2), e2021GL097420. <https://doi.org/10.1029/2021GL097420>
- Fasullo, J. T., Phillips, A. S., & Deser, C. (2020). Evaluation of leading modes of climate variability in the CMIP archives. *Journal of Climate*, 33(13), 5527–5545. <https://doi.org/10.1175/JCLI-D-19-1024.1>
- Fournier, S., Willis, J., Killett, E., Qu, Z., & Zlotnicki, V. (2022). JPL MEEA-SUREs gridded Sea Surface height anomalies version 2205. Ver. 2205 PO.DAAC, CA, USA [Dataset]. <https://doi.org/10.5067/SLREF-CDRV3>
- Freeman, N. M., Lovenduski, N. S., & Gent, P. R. (2016). Temporal variability in the Antarctic Polar Front (2002–2014). *Journal of Geophysical Research: Oceans*, 121(10), 7263–7276. <https://doi.org/10.1002/2016JC012145>
- Gelaro, R., McCarty, W., Suarez, M. J., Todling, R., Molod, A., Takacs, L., et al. (2017). The Modern-Era Retrospective Analysis for Research and Applications, version 2 (MERRA-2). *Journal of Climate*, 30(14), 5419–5454. <https://doi.org/10.1175/JCLI-D-16-0758.1>
- Gille, S. T. (2014). Meridional displacement of the Antarctic circumpolar current. *Philos. Trans. R. Soc. A*, 372(2019), 20130273. <https://doi.org/10.1098/rsta.2013.0273>
- Gregory, J. M., Griffies, S. M., Hughes, C. W., Lowe, J. A., Church, J. A., Fukimori, I., et al. (2019). Concepts and terminology for Sea Level: Mean, variability and change, both local and global. *Surveys in Geophysics*, 40(6), 1251–1289. <https://doi.org/10.1007/s10712-019-09525-z>
- Hamlington, B. D., Fasullo, J. T., Nerem, R. S., Kim, K. Y., & Landerer, F. W. (2019). Uncovering the pattern of forced Sea Level rise in the satellite altimeter record. *Geophysical Research Letters*, 46(9), 4844–4853. <https://doi.org/10.1029/2018GL081386>
- Hamlington, B. D., Frederikse, T., Thompson, P. R., Willis, J. K., Nerem, R. S., & Fasullo, J. T. (2021). Past, present, and future Pacific sea-level change. *Earth's Future*, 8(4), e2020EF001839. <https://doi.org/10.1029/2020EF001839>
- Han, W., Stammer, D., Meehl, G. A., Hu, A., Sienz, F., & Zhang, L. (2018). Multi-decadal trend and decadal variability of the regional Sea Level over the Indian Ocean since the 1960s: Roles of climate modes and external forcing. *Climate*, 6(2), 51. <https://doi.org/10.3390/clif6020051>
- Heede, U. K., & Fedorov, A. V. (2021). Eastern equatorial Pacific warming delayed by aerosols and thermostat response to CO<sub>2</sub> increase. *Nature Climate Change*, 11(8), 696–703. <https://doi.org/10.1038/s41558-021-01101-x>
- Hersbach, H., Bell, B., Berrisford, P., Hirahara, S., Horányi, A., Muñoz-Sabater, J., et al. (2020). The ERA5 global reanalysis. *Quarterly Journal of the Royal Meteorological Society*, 146(730), 1999–2049. <https://doi.org/10.1002/qj.3803>
- Holbrook, N. J., Scannell, H. A., Sen Gupta, A., Benthuysen, J. A., Feng, M., Oliver, E. C. J., et al. (2019). A global assessment of marine heatwaves and their drivers. *Nature Communications*, 10, 1–13. <https://doi.org/10.1038/s41467-019-10206-z>
- Huang, B., Liu, C., Banzon, V., Freeman, E., Graham, G., Hankins, B., et al. (2021). Improvements of the Daily Optimum Interpolation Sea Surface Temperature (DOISST) version 2.1. *Journal of Climate*, 34(8), 2923–2939. <https://doi.org/10.1175/JCLI-D-20-0166.1>
- Hurrell, J. W., Holland, M. M., Gent, P. R., Ghan, S., Kay, J. E., Kushner, P. J., et al. (2013). The community Earth system model: A framework for collaborative research. *Bulletin America Meteorology Social*, 94(9), 1339–1360. <https://doi.org/10.1175/BAMS-D-12-00121.1>
- Joh, Y., & Di Lorenzo, E. (2017). Increasing coupling between NPGO and PDO leads to prolonged marine heatwaves in the northeast pacific. *Geophysical Research Letters*, 44(22), 11–663. <https://doi.org/10.1002/2017gl075930>
- Jousset, S., Mulet, S., Wilkin, J., Greiner, E., Dibarboire, G., & Picot, N. (2022). New global Mean Dynamic Topography CNES-CLS-22 combining drifters, hydrological profiles and High Frequency radar data. *OSTST*. <https://doi.org/10.24400/527896/a03-2022.3292>
- Karnauskas, K. B., Heede, U. K., & Zhang, L. (2023). The impact of eastern Pacific warming on future North Atlantic tropical cyclogenesis. *Geophysical Research Letters*, 50(17), e2023GL105551. <https://doi.org/10.1029/2023GL105551>
- Karnauskas, K. B., Seager, R., Kaplan, A., Kushnir, Y., & Cane, M. A. (2009). Observed strengthening of the zonal sea surface temperature gradient across the equatorial Pacific Ocean. *Journal of Climate*, 22(16), 4316–4321. <https://doi.org/10.1175/2009JCLI2936.1>
- Kay, J. E., & Coauthors (2015). The Community Earth System Model (CESM) large ensemble project: A community resource for studying climate change in the presence of internal climate variability. *Bulletin America Meteorology Social*, 96, 1333–1349. <https://doi.org/10.1175/BAMS-D-13-00255.1>
- Lee, S., & Feldstein, S. B. (2013). Detecting ozone- and greenhouse gas–driven wind trends with observational data. *Science*, 339(61190), 563–567. <https://doi.org/10.1126/science.1225154>
- Lee, S., L'Heureux, M., Wittenberg, A. T., Seager, R., O'Gorman, P. A., & Johnson, N. C. (2022). On the future zonal contrasts of equatorial Pacific climate: Perspectives from Observations, Simulations, and Theories. *npj Climate and Atmospheric Science*, 5(1), 82. <https://doi.org/10.1038/s41612-022-00301-2>
- Lindzen, R. S., & Nigam, S. (1987). On the role of sea surface temperature gradients in forcing low-level winds and convergence in the tropics. *Journal of the Atmospheric Sciences*, 44(17), 2418–2436. [https://doi.org/10.1175/1520-0469\(1987\)044,2418:OTROSS.2.0.CO;2](https://doi.org/10.1175/1520-0469(1987)044,2418:OTROSS.2.0.CO;2)
- Lu, J., Vecchi, G. A., & Reichler, T. (2007). Expansion of the Hadley cell under global warming. *Geophysical Research Letters*, 34(6), L06805. <https://doi.org/10.1029/2006GL028443>
- Merrifield, M. A. (2011). A shift in western tropical pacific Sea Level trends during the 1990s. *Journal of Climate*, 24(15), 4126–4138. <https://doi.org/10.1175/2011JCLI3932.1>
- Mitrovica, J. X., Gomez, N., & Clark, P. U. (2009). The sea-level fingerprint of West Antarctic collapse. *Science*, 323(5915), 753. <https://doi.org/10.1126/science.1166510>
- Mitrovica, J. X., Tamisiea, M. E., Davis, J. L., & Milne, G. A. (2001). Recent mass balance of polar ice sheets inferred from patterns of global sea-level change. *Nature*, 409(6823), 1026–1029. <https://doi.org/10.1038/35059054>
- Nicholls, R. J., & Cazenave, A. (2010). Sea-level rise and its impact on coastal zones. *Science*, 328(5985), 1517–1520. <https://doi.org/10.1126/science.1185782>
- Otosaka, I. N., Shepherd, A., Ivins, E. R., Schlegel, N. J., Amory, C., van den Broeke, M. R., et al. (2023). Mass balance of the Greenland and Antarctic ice sheets from 1992 to 2020. *Earth System Science Data*, 15(4), 1597–1616. <https://doi.org/10.5194/essd-15-1597-2023>
- Paulson, A., Zhong, S., & Wahr, J. (2005). Modelling post-glacial rebound with lateral viscosity variations. *Geophysical Journal International*, 163(1), 357–371. <https://doi.org/10.1111/j.1365-246X.2005.02645.x>
- Peyser, C. E., Yin, J., Landerer, F. W., & Cole, J. E. (2016). Pacific sea level rise patterns and global surface temperature variability. *Geophysical Research Letters*, 43(16), 8662–8669. <https://doi.org/10.1002/2016GL069401>
- Richter, K., Meyssignac, B., Slanget, A. B., Melet, A., Church, J. A., Fettweis, X., et al. (2020). Detecting a forced signal in satellite-era sea-level change. *Environmental Research Letters*, 15(9), 094079. <https://doi.org/10.1088/1748-9326/ab986e>
- Rodgers, K. B., Lee, S.-S., Rosenbloom, N., Timmermann, A., Timmermann, G., Deser, C., et al. (2021). Ubiquity of human-induced changes in climate variability. *Earth System Dynamics*, 12(4), 1393–1411. <https://doi.org/10.5194/esd-12-1393-2021>

- Rounce, D. R., Hock, R., Maussion, F., Hugonnet, R., Kochtitzky, W., Huss, M., et al. (2023). Global glacier change in the 21st century: Every increase in temperature matters. *Science*, 379(6627), 78–83. <https://doi.org/10.1126/science.abo1324>
- Royston, S., Watson, C. S., Legrèsy, B., King, M. A., Church, J. A., & Bos, M. S. (2018). Sea-level trend uncertainty with Pacific climatic variability and temporally-correlated noise. *Journal of Geophysical Research: Oceans*, 123(3), 1978–1993. <https://doi.org/10.1002/2017JC013655>
- Rugenstein, M., Zelinka, M., Karnauskas, K. B., Ceppi, P., & Andrews, T. (2023). Patterns of surface warming matter for climate sensitivity. *Eos*, 104. <https://doi.org/10.1029/2023EO230411>
- Saenko, O. A., Fyfe, J. C., & England, M. H. (2005). On the response of the oceanic wind-driven circulation to atmospheric CO<sub>2</sub> increase. *Climate Dynamics*, 25(4), 415–426. <https://doi.org/10.1007/s00382-005-0032-5>
- Sallenger, A., Doran, K., & Howd, P. (2012). Hotspot of accelerated sea-level rise on the Atlantic coast of North America. *Nature Climate Change*, 2(12), 884–888. <https://doi.org/10.1038/nclimate1597>
- Samanta, D., Vairagi, V., Richter, K., McDonagh, E. L., Karnauskas, K. B., Goodkin, N. F., et al. (2024). The role of anthropogenic forcings on historical sea-level change in the Indo-Pacific warm pool region. *Earth's Future*, 12(3), e2023EF003684. <https://doi.org/10.1029/2023EF003684>
- Schloesser, F., Thompson, P. R., & Piecuch, C. G. (2021). Meridional asymmetry in recent decadal sea-level trends in the subtropical Pacific Ocean. *Geophysical Research Letters*, 48(6), e2020GL091959. <https://doi.org/10.1029/2020GL091959>
- Seager, R., & Simpson, I. R. (2016). Western boundary currents and climate change. *Journal of Geophysical Research: Oceans*, 121(9), 7212–7214. <https://doi.org/10.1002/2016JC012156>
- Seager, R., Henderson, N., & Cane, M. (2022). Persistent discrepancies between observed and modeled trends in the tropical Pacific Ocean. *Journal of Climate*, 35(14), 4571–4584. <https://doi.org/10.1175/JCLI-D-21-0648.1>
- Seidel, D. J., Fu, Q., Randel, W. J., & Reichler, T. J. (2008). Widening of the tropical belt in a changing climate. *Nature Geoscience*, 1(1), 21–24. <https://doi.org/10.1038/ngeo.2007.38>
- Sérazin, G., Meyssignac, B., Penduff, T., Terray, L., Barnier, B., & Molines, J.-M. (2016). Quantifying uncertainties on regional sea level change induced by multidecadal intrinsic oceanic variability. *Geophysical Research Letters*, 43(15), 8151–8159. <https://doi.org/10.1002/2016GL069273>
- Shi, H., García-Reyes, M., Jacox, M. G., Rykaczewski, R. R., Black, B. A., Bograd, S. J., & Sydeman, W. J. (2021). Co-occurrence of California drought and northeast Pacific marine heatwaves under climate change. *Geophysical Research Letters*, 48(17), e2021GL092765. <https://doi.org/10.1029/2021GL092765>
- Simpson, I. R., & Coauthors (2023). The CESM2 single-forcing large ensemble and comparison to CESM1: Implications for experimental design. *Journal of Climate*, 36, 5687–5711. <https://doi.org/10.1175/JCLI-D-22-0666.1>
- Simpson, I., Shaw, T., & Seager, R. (2014). A diagnosis of the seasonally and longitudinally varying mid-latitude circulation response to global warming. *Journal of the Atmospheric Sciences*, 71(7), 2489–2515. <https://doi.org/10.1175/jas-d-13-0325.1>
- Sobel, A. H., Lee, C.-Y., Bowen, S. G., Camargo, S. J., Cane, M. A., Clement, A., et al. (2023). Near-term tropical cyclone risk and coupled Earth system model biases. *Proceedings of the National Academy of Sciences of the United States of America*, 120(33). <https://doi.org/10.1073/pnas.2209631120>
- Sokolov, S., & Rintoul, S. R. (2009). Circumpolar structure and distribution of the Antarctic Circumpolar Current fronts: 2. Variability and relationship to sea surface height. *Journal of Geophysical Research*, 114(C11), C11019. <https://doi.org/10.1029/2008JC005248>
- Stammer, D., Cazenave, A., Ponte, R. M., & Tamisiea, M. E. (2013). Causes for Contemporary Regional Sea Level Changes. *Annual Review of Marine Science*, 5(1), 21–46. <https://doi.org/10.1146/annurev-marine-121211-172406>
- Sweet, W. V., Kopp, R. E., Weaver, C. P., Obeysekera, J., Horton, R. M., Thieler, E. R., & Zervas, C. (2017). Global and regional sea level rise scenarios for the United States. NOAA Technical Report NOS CO-OPS 083. <https://doi.org/10.7289/V5/TR-NOS-COOPS-083>
- Tamisiea, M. E. (2011). Ongoing glacial isostatic contributions to observations of sea level change. *Geophysical Journal International*, 186(3), 1036–1044. <https://doi.org/10.1111/j.1365-246X.2011.05116.x>
- Thompson, P. R., Piecuch, C. G., Merrifield, M. A., McCreary, J. P., & Firing, E. (2016). Forcing of recent decadal variability in the Equatorial and North Indian Ocean. *Journal of Geophysical Research: Oceans*, 121(9), 6762–6778. <https://doi.org/10.1002/2016JC012132>
- Timmermann, A., McGregor, S., & Jin, F. (2010). Wind effects on past and future Regional Sea Level trends in the Southern Indo-Pacific. *Journal of Climate*, 23(16), 4429–4437. <https://doi.org/10.1175/2010JCLI3519.1>
- Todd, A., Zanna, L., Couldrey, M., Gregory, J., Wu, Q., Church, J. A., et al. (2020). Ocean-only FAFMIP: Understanding regional patterns of ocean heat content and dynamic sea level change. *Journal of Advances in Modeling Earth Systems*, 12(8), e2019MS002027. <https://doi.org/10.1029/2019MS002027>
- Walker, J. S., Kopp, R. E., Shaw, T. A., Cahill, N., Khan, N. S., Barber, D. C., et al. (2021). Common Era sea-level budgets along the U.S. Atlantic coast. *Nature Communications*, 12(1), 1841. <https://doi.org/10.1038/s41467-021-22079-2>
- Wills, R. C. J., Dong, Y., Proistosecu, C., Armour, K. C., & Battisti, D. S. (2022). Systematic climate model biases in the large-scale patterns of recent sea-surface temperature and sea-level pressure change. *Geophysical Research Letters*, 49(17), e2022GL100011. <https://doi.org/10.1029/2022GL100011>
- Yang, H., Lohmann, G., Krebs-Kanzow, U., Ionita, M., Shi, X., Sidorenko, D., et al. (2020). Poleward shift of the major ocean gyres detected in a warming climate. *Geophysical Research Letters*, 47(5), e2019GL085868. <https://doi.org/10.1029/2019GL085868>
- Yang, H., Lohmann, G., Wei, W., Dima, M., Ionita, M., & Liu, J. (2016). Intensification and poleward shift of subtropical western boundary currents in a warming climate. *Journal of Geophysical Research: Oceans*, 121(7), 4928–4945. <https://doi.org/10.1002/2015JC011513>
- Yin, J. (2005). A consistent poleward shift of the storm tracks in simulations of 21st century climate. *Geophysical Research Letters*, 32(18), L18701. <https://doi.org/10.1029/2005GL023684>